Advances in Chemical Physics

Volume 161

all-atom
system

coarse-grained
hydrogens

coarse-grained
functional groups

coarse-grained
amino acid residues

Edited by

Stuart A. Rice and Aaron R. Dinner

WILEY

ADVANCES IN CHEMICAL PHYSICS

VOLUME 161

ADVANCES IN CHEMICAL PHYSICS

VOLUME 161

Edited by

Stuart A. Rice

Department of Chemistry
and
The James Franck Institute,
The University of Chicago,
Chicago, IL, USA

Aaron R. Dinner

Department of Chemistry
and
The James Franck Institute,
The University of Chicago,
Chicago, IL, USA

WILEY

EDITORIAL BOARD

CONTENTS

CONTRIBUTORS TO VOLUME 161

MASSIMO ALTARELLI, European XFEL GmbH, Schenefeld, Germany

WILLIAM T. COFFEY, Department of Electronic and Electrical Engineering, Trinity College, Dublin, Ireland

JACK F. DOUGLAS, Materials Science and Engineering Division, National Institute of Standards and Technology, Gaithersburg, MD, USA

KARL F. FREED, James Franck Institute and Department of Chemistry, The University of Chicago, Chicago, IL, USA

YURI P. KALMYKOV, Laboratoire de Mathématiques et Physique (LAMPS, EA 4217), Université de Perpignan Via Domitia, Perpignan, France

JOHN J. KOZAK, Department of Chemistry, DePaul University, Chicago, IL, USA

RUSLAN P. KURTA, European XFEL GmbH, Schenefeld, Germany

GEORGE D. J. PHILLIES, Department of Physics, Worcester Polytechnic Institute, Worcester, MA, USA

JAROSLAW PIASECKI, Institute of Theoretical Physics, Faculty of Physics, University of Warsaw, Warsaw, Poland

M. SCOTT SHELL, Department of Chemical Engineering, University of California Santa Barbara, Santa Barbara, CA, USA

SAMANVAYA SRIVASTAVA, Institute for Molecular Engineering, The University of Chicago, Chicago, IL, USA

PIOTR SZYMCZAK, Institute of Theoretical Physics, Faculty of Physics, University of Warsaw, Warsaw, Poland

MATTHEW V. TIRRELL, Institute for Molecular Engineering, The University of Chicago, Chicago, IL, USA

SERGUEY V. TITOV, Kotel'nikov Institute of Radio Engineering and Electronics of the Russian Academy of Sciences, Moscow, Russian Federation

IVAN A. VARTANYANTS, Deutsches Elektronen-Synchrotron, DESY, Hamburg, Germany; National Research Nuclear University 'MEPhI' (Moscow Engineering Physics Institute), Moscow, Russia

WEN-SHENG XU, James Franck Institute, The University of Chicago, Chicago, IL, USA

PREFACE TO THE SERIES

Advances in science often involve initial development of individual specialized fields of study within traditional disciplines followed by broadening and overlap, or even merging, of those specialized fields, leading to a blurring of the lines between traditional disciplines. The pace of that blurring has accelerated in the past few decades, and much of the important and exciting research carried out today seeks to synthesize elements from different fields of knowledge. Examples of such research areas include biophysics and studies of nanostructured materials. As the study of the forces that govern the structure and dynamics of molecular systems, chemical physics encompasses these and many other emerging research directions. Unfortunately, the flood of scientific literature has been accompanied by losses in the shared vocabulary and approaches of the traditional disciplines, and there is much pressure from scientific journals to be ever more concise in the descriptions of studies, to the point that much valuable experience, if recorded at all, is hidden in supplements and dissipated with time. These trends in science and publishing make this series, *Advances in Chemical Physics*, a much needed resource.

The *Advances in Chemical Physics* is devoted to helping the reader obtain general information about a wide variety of topics in chemical physics, a field that we interpret very broadly. Our intent is to have experts present comprehensive analyses of subjects of interest and to encourage the expression of individual points of view. We hope that this approach to the presentation of an overview of a subject will both stimulate new research and serve as a personalized learning text for beginners in a field.

STUART A. RICE
AARON R. DINNER
January 2016, Chicago, IL, USA

STRUCTURAL ANALYSIS BY X-RAY INTENSITY ANGULAR CROSS CORRELATIONS

RUSLAN P. KURTA[1], MASSIMO ALTARELLI[1],
and IVAN A. VARTANYANTS[2,3]

[1]*European XFEL GmbH, Schenefeld, Germany*
[2]*Deutsches Elektronen-Synchrotron, DESY, Hamburg, Germany*
[3]*National Research Nuclear University 'MEPhI' (Moscow Engineering Physics Institute), Moscow, Russia*

CONTENTS

I. INTRODUCTION

The aim of this chapter is to review the topic of angular intensity correlations in X-ray diffraction. This topic has a history going back by almost 40 years, and is intertwined with developments in the related areas of intensity correlations in optical laser scattering and in electron scattering; but it has recently known a revival, partly related to the progress in X-ray sources and in instrumentation.

In the early literature, scattering experiments performed on randomly oriented objects in a solution were mostly discussed. Correlations between scattered intensity $I(\mathbf{q}, t)$ in different directions (for different scattering vectors $\mathbf{q}$) at the same or at different times t were considered,

$$C(\mathbf{q}_1, \mathbf{q}_2, t, t') \sim \langle I(\mathbf{q}_1, t) I(\mathbf{q}_2, t') \rangle, \tag{1}$$

where the brackets indicate an average over many measurements. In the case of light scattering [1, 2], a laser source was generally used and its full transverse coherence always implies an interference between the scattering by different particles inside the scattering volume. Also, rather large particles of the order of hundreds of nanometers, matching the wavelength of light, were investigated, in a concentration such that the average number of particles within the illuminated volume (defined by apertures) was rather small. The large particle size and the intensity of laser light combine to achieve an exposure time shorter than the characteristic orientational relaxation time of the objects. In the pioneering work by Kam [3], the intensity correlations between scattering of X-rays or neutrons from macromolecules in solution were addressed, also in the limit in which the data could be acquired in a time shorter than the characteristic molecular reorientation time. The possibility of this correlation analysis to obtain structural information without crystallization was proposed. Similar concepts were applied to electron microscopy; see, for example, Refs. 4 and 5.

The conventional X-ray scattering pattern of a disordered system, for example, a liquid, molecules in solution, or an amorphous solid is isotropic (Debye–Scherrer rings) when recorded with a weak, and low coherence, source [6, 7]. The weak source, in contrast to the previously discussed examples, means that the exposure time required to collect a sufficient signal, in the case of a liquid or a solution, is long compared to characteristic relaxation times of the rotational and translational agitation. If, on the other hand, the signal can be acquired in a short time with a brilliant X-ray source with a high degree of coherence, such as available with a third-generation synchrotron source or X-ray free-electron laser, the recorded pattern is not isotropic, but is an apparently random collection of speckles. These speckles are in fact encoding the instantaneous positions and orientations of the molecules. In an amorphous solid, in a random alloy or in a glass, with slow dynamics, on the other hand, the duration of the exposure is not so relevant, but a source with a high degree of partial coherence can here also reveal a speckle pattern encoding local fluctuations in orientation or ordering.

Due to high penetration of X-rays, multiple scattering effects on a disordered sample of few microns size can be safely neglected and kinematical scattering will be assumed to be valid. This is a very important simplification of the theory that is valid only for a limited number of samples studied by visible light or by electrons, where multiple scattering effects can seldom be neglected. This makes X-rays especially attractive for the study of disordered systems. A low-noise, high-dynamic range detector, with sufficient angular resolution, is also needed to record meaningful angular anisotropies. The very recent emergence of X-ray free-electron lasers (XFELs) [8–10], with ultrabright pulses of few femtoseconds duration and a high degree of transverse coherence, is opening up the promise of a completely new set of experimental conditions and provides further motivation for exploring the potential benefits of correlation analysis.

The revival of angular correlation studies was recently prompted by the work of Wochner et al. [11], which reported angular correlations with pronounced periodic character in a colloidal suspension of polymethylmethacrylate (PMMA) spheres, expected to form icosahedral clusters near the glass formation concentration. They considered angular averages in the form of a cross-correlation function (CCF) calculated on the same scattering ring ($|q_1| = |q_2| = q$) and at the same time $t = t'$ (the scattering vector $\mathbf{q}$, in the plane normal to the incoming beam, being expressed as $\mathbf{q} \equiv (q, \varphi)$)

$$C(q, \Delta) = \frac{\langle \widetilde{I}(q, \varphi)\widetilde{I}(q, \varphi + \Delta)\rangle_\varphi}{\langle I(q, \varphi)\rangle_\varphi^2}, \tag{2}$$

where $0 \leq \Delta \leq 2\pi$ is the angular coordinate, $\widetilde{I}(q, \varphi) = I(q, \varphi) - \langle I(q, \varphi)\rangle_\varphi$ is the intensity fluctuation, function, and $\langle f(\varphi)\rangle_\varphi = (1/2\pi) \int_0^{2\pi} f(\varphi)d\varphi$ denotes the average over the angle φ. This work stimulated further theoretical [12–21] and experimental [22–31] exploration of the CCFs in the studies of disordered materials by X-ray scattering, as well as light [32] and electron scattering [33].

There are two main scientific drivers for the investigation of the angular correlations of X-ray scattering patterns. On the one hand, the angular correlations in scattering experiments are investigated *as a possible tool to solve structures of molecules in solutions* or, more generally, in noncrystalline systems (see Fig. 1). This line of thought, as we saw, goes back to the work of Kam [3], almost 40 years ago; his seminal (although so far not yet implemented in full) idea, was that the intensity fluctuations contain additional information, with respect to the average around the scattering intensity rings. This could allow to go beyond the quantities traditionally extracted from the isotropic patterns (average pair correlation functions in a liquid, or radius of gyrations for molecules in solutions, etc.), possibly all the way to the high-resolution molecular structure. In the more recent applications, the progress in instrumentation opens the door to a rapid acquisition of many scattering patterns; this makes acquisition of angular correlations not only in each diffraction pattern but also over an ensemble of many diffraction patterns possible [3, 34].
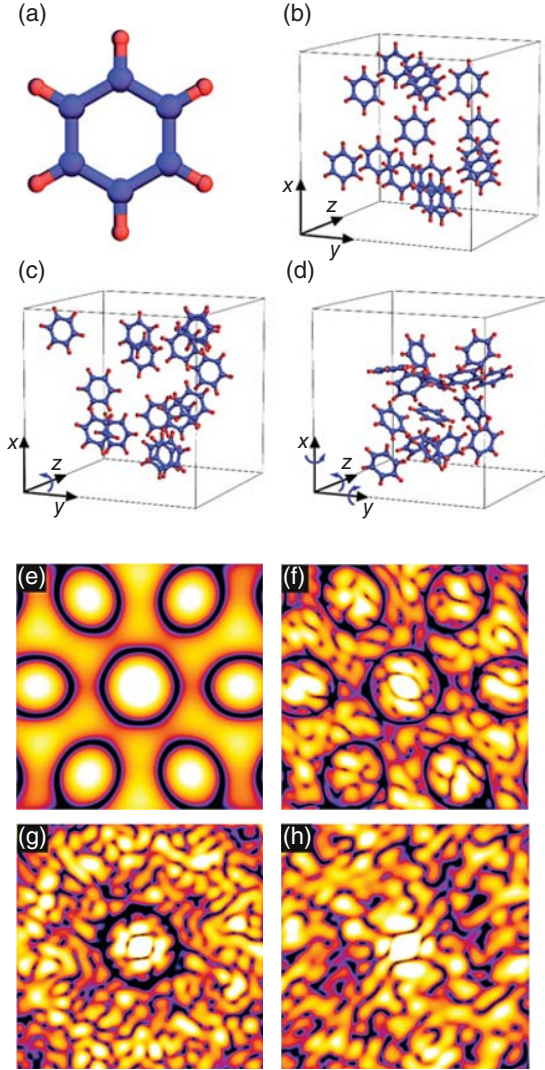
Figure 1. Different types of structural disorder in a system of particles recorded by coherent X-ray snapshots. (a) A single benzene-like molecule and the corresponding simulated coherent diffraction pattern (e). (b) Oriented system of molecules, where particles have random positions but the same orientation as the molecule shown in (a). Corresponding scattering pattern (f) encodes information about a single-particle structure (compare with (e)), modulated by coherent superposition of waves scattered from molecules in different positions. (c) Aligned system of molecules, where in addition to positional disorder particles have random orientations about z-axis. Only the central part of the respective scattering pattern (g) reminds about the single-molecule diffraction pattern (a). (d) Completely disordered system of molecules, where particles have random positions and orientations. Scattering pattern simulated for this system can not be directly associated with the single molecule. In all simulations direction of the incoming beam is assumed along z-axis. (*See insert for color representation of the figure.*)

On the other hand, an alternative application of angular correlations could be very important for the physics of disordered or partially ordered systems: *it is the unveiling of hidden symmetries and of partial order*. This includes systems displaying short-range order (SRO) [35, 36], as well as complicated dynamics, aging, dynamical heterogeneity, and medium-range order (MRO) in a large class of glass-forming liquids [37–41]. In such systems, a relevant question is, for example, if one can recognize and identify an *n*-fold symmetry axis of an individual molecular species from the diffraction patterns of a liquid composed of such molecules, can bond angles be detected from the study of angular fluctuations of the diffracted intensity of an amorphous system? Encouraging results were in fact obtained in the study of partially ordered quasi two-dimensional (2D) systems, like liquid crystals [42–45] in which hexatic bond-orientational (BO) order can be detected by the study of the angular dependence of the diffracted intensity. More generally, the study of BO order, characterized by the order parameter quantitatively defined in the pioneering work of Steinhardt et al. [35], is also an obvious target for the study of angular correlations.

The structure of this Chapter is as follows. A basic theoretical description of quantities related to angular correlations in a simple X-ray scattering description in the far-field, or Fraunhofer, limit of diffraction in the kinematic approximation is given in Section II. Despite these simplifying assumptions, this analysis shall allow us to draw general conclusions on the nature of the measured correlation functions, on the role of the coherence length of the incoming X-rays, and of the dilution of the physical system under investigation; and to investigate possible approaches toward the two main scientific target areas outlined above for such studies. In Section III, a survey of recent numerical and experimental work is critically discussed. In Section IV, we provide a summary and outlook of the angular cross-correlation methods and their future applications.

II. THEORY

A. Scattering from a Disordered System of Reproducible Particles

We will consider in the following a scattering experiment in transmission geometry as shown in Figure 2a. An incident coherent X-ray beam scatters from a disordered sample, and the resulting speckle pattern is measured on a 2D detector in the far-field. As a general model system, we consider a 3D sample consisting of N identical particles with random positions and orientations (see Fig. 2). The particles itself could, in principle, represent a complicated but reproducible structure. This model includes a variety of systems, for example, clusters or molecules in the gas phase, local structures formed in colloidal systems, viruses in solution, etc.

The amplitude $A_k(\mathbf{q})$ scattered from the k-th particle at the momentum transfer vector $\mathbf{q}$ can be defined as [47]

$$A_k(\mathbf{q}) = \int \rho_k(\mathbf{r}) e^{i\mathbf{q}\cdot\mathbf{r}} d\mathbf{r}, \qquad (3)$$
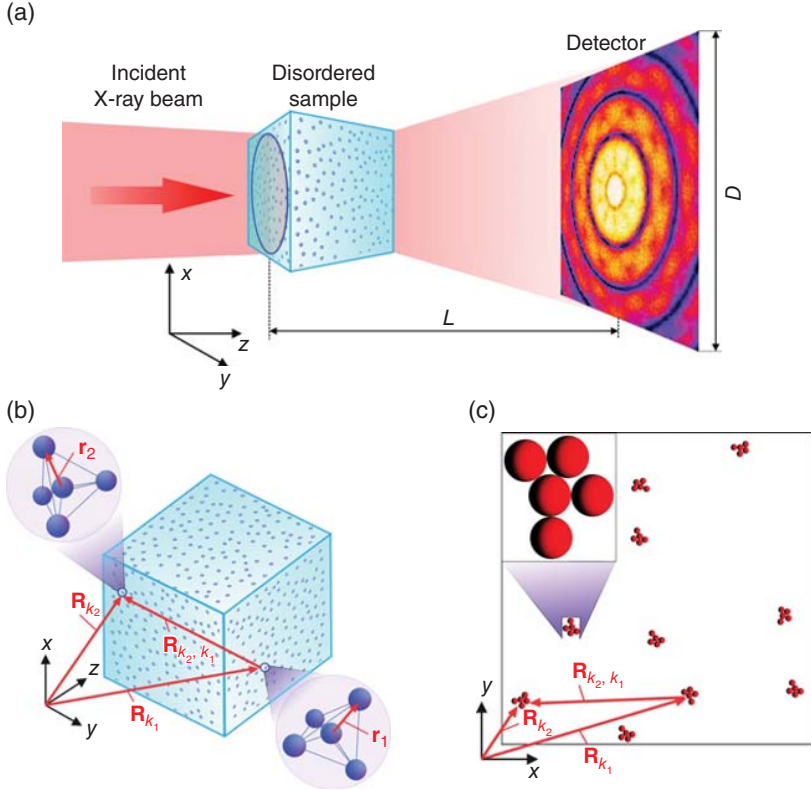
Figure 2. (a) Geometry of the diffraction experiment. A coherent X-ray beam illuminates a disordered sample and produces a diffraction pattern on a detector. The direction of the incident beam is defined along the z-axis of the coordinate system. (b) A disordered 3D sample composed of tetrahedral pentamers. All clusters have random position and orientation in the 3D space. (c) A disordered 2D sample composed of asymmetric clusters. All clusters have random position and orientation in the 2D plane. Reproduced from Ref. 46. Used under CC By 3.0, http://creativecommons.org/licenses/by/3.0/.

where $\rho_k(\mathbf{r})$ is an electron density of the k-th particle (see Fig. 2b) and the integration is performed over the volume of the particle. Using Eq. (3), the intensity $I(\mathbf{q})$ coherently scattered from a disordered sample consisting of N particles at the position $\mathbf{R}_k$ is given by

$$
\begin{aligned}
I(\mathbf{q}) &= \sum_{k_1,k_2=1}^{N} e^{i\mathbf{q}\cdot\mathbf{R}_{k_2,k_1}} A_{k_1}^*(\mathbf{q}) A_{k_2}(\mathbf{q}) \\
&= \sum_{k_1,k_2=1}^{N} \int\int \rho_{k_1}^*(\mathbf{r}_1)\rho_{k_2}(\mathbf{r}_2) e^{i\mathbf{q}\cdot\mathbf{R}_{k_2,k_1}^{21}} d\mathbf{r}_1 d\mathbf{r}_2,
\end{aligned}
\qquad (4)
$$

where the double summation is performed over all N particles, and the integration is performed over the volume of the k_i-th particle ($i = 1, 2$). Here, the following notation for the radius vectors is used, $\mathbf{R}^{21}_{k_2,k_1} = \mathbf{R}_{k_2,k_1} + \mathbf{r}_{21}$, where $\mathbf{R}_{k_2,k_1} = \mathbf{R}_{k_2} - \mathbf{R}_{k_1}$ is the vector connecting two different particles k_1 and k_2, and $\mathbf{r}_{21} = \mathbf{r}_2 - \mathbf{r}_1$, where the vectors $\mathbf{r}_1$ and $\mathbf{r}_2$ are local coordinates inside the particles k_1 and k_2, respectively (see Fig. 2b and c).

In the case of a partially coherent illumination and a dilute disordered system when the mean distance between the particles is larger than the coherence length of the incoming beam, the interparticle correlations due to coherent interference of scattered amplitudes from the individual particles in Eq. (4) can be neglected. In these conditions, the total scattered intensity $I(\mathbf{q})$ can be represented as a sum of intensities $I_k(\mathbf{q}) = |A_k(\mathbf{q})|^2$ corresponding to individual particles in the system

$$I(\mathbf{q}) = \sum_{k=1}^{N} I_k(\mathbf{q}). \tag{5}$$

In the following, we will use Fourier decomposition of the scattered intensity $I(q, \varphi)$ on the ring of radius q (see Fig. 3a),

$$I(q, \varphi) = \sum_{n=-\infty}^{\infty} I_q^n e^{in\varphi}, \tag{6a}$$

$$I_q^n = \frac{1}{2\pi} \int_0^{2\pi} I(q, \varphi) e^{-in\varphi} d\varphi, \tag{6b}$$

where I_q^n are the components of the Fourier decomposition. Since scattered intensities are always real quantities, it is easy to show that $I_q^{-n} = I_q^{n*}$. By its definition, the 0th-order Fourier component represents an angular averaged intensity, $I_q^0 = \langle I(q, \varphi) \rangle_\varphi$.

Here, we would like to note that different authors are using different basic functions for decomposition of the scattered intensities. These are, for example, spherical harmonics [3, 25, 34, 48–52], icosahedral harmonics [15], and 3D Zernike polynomials [17, 53]. The choice of decomposition is often dictated by the symmetry of particles and helps to reduce the number of variables, or unknown parameters.

B.   2D Disordered Systems

In this section, we consider the particular case of a 2D system in a small-angle scattering geometry with a flat Ewald sphere, when all coordinate vectors are defined in a 2D plane (see Fig. 2c), and the electron density of the k-th particle transforms to a projected electron density, $\widetilde{\rho}_k(\mathbf{r}) = \int \rho_k(\mathbf{r}, z) dz$. We would like to note here that in the case of plane wavefront illumination of a 2D system, only even ($n = 2l, l = 1, 2, 3, \ldots$) Fourier components of the intensity I_q^n can have nonzero values [12, 13].
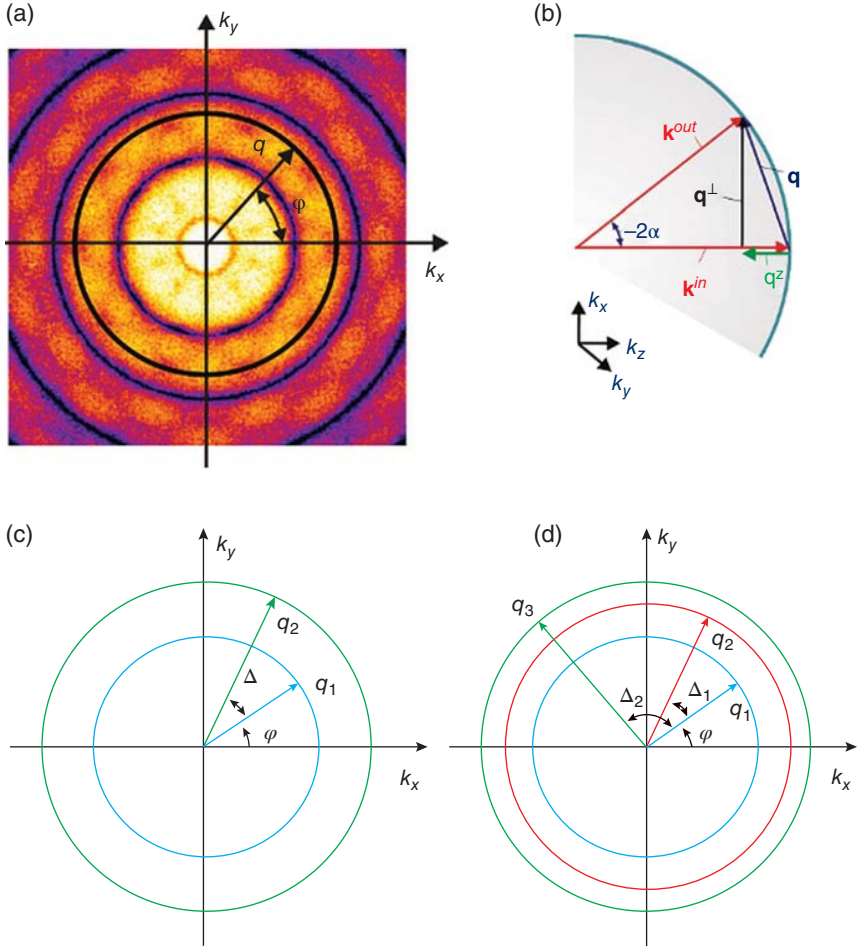
Figure 3. Scattering geometry in reciprocal space. (a) Scattered intensity $I(\mathbf{q})$ defined in the detector plane in the polar coordinate system, $\mathbf{q} = (q, \varphi)$. (b) Ewald sphere construction. Here, $\mathbf{k}^{in}$ is the wavevector of the incident beam directed along the z-axis, $\mathbf{k}^{out}$ is the wavevector of the scattered wave with the scattering angle 2α. The scattering vector $\mathbf{q} = (\mathbf{q}^{\perp}, q^z)$ is decomposed into two components that are perpendicular $\mathbf{q}^{\perp}$ and parallel q^z to the direction of the incident beam. (c and d) Momentum transfer vectors used in the definition of the two-point $C(q_1, q_2, \Delta)$ (c), and three-point CCFs $C(q_1, q_2, q_3, \Delta_1, \Delta_2)$ (d). Reproduced from Ref. 46. Used under CC By 3.0, http://creativecommons.org/licenses/by/3.0/.

1. Dilute Systems

First, we consider scattering from a single particle in a disordered system. The intensity $I_{\psi_0}(\mathbf{q})$ scattered from such a particle in some reference orientation ψ_0 is related to the projected electron density of the particle $\widetilde{\rho}_{\psi_0}(\mathbf{r})$ through its scattered amplitude (Eq. 3) as $I_{\psi_0}(\mathbf{q}) = |A_{\psi_0}(\mathbf{q})|^2$. Similar to $I(\mathbf{q})$ (see Eq. 6a and b), the intensity $I_{\psi_0}(\mathbf{q}) \equiv I_{\psi_0}(q, \varphi)$ can be represented as an angular Fourier series expansion,

$$I_{\psi_0}(q, \varphi) = \sum_{n=-\infty}^{\infty} I_{q,\psi_0}^n e^{in\varphi}, \tag{7}$$

where I_{q,ψ_0}^n are the Fourier components of $I_{\psi_0}(q, \varphi)$.

The Fourier component I_{q,ψ_0}^n is related to the projected electron density $\widetilde{\rho}_{\psi_0}(\mathbf{r})$ of the particle as [12, 13, 16]

$$I_{q,\psi_0}^n = \int \int \widetilde{\rho}_{\psi_0}^*(\mathbf{r}_1) \widetilde{\rho}_{\psi_0}(\mathbf{r}_2) J_n(q|\mathbf{r}_{21}|) e^{-in\phi_{\mathbf{r}_{21}}} \, d\mathbf{r}_1 d\mathbf{r}_2, \tag{8}$$

where $\phi_{\mathbf{r}_{21}}$ is the angle of the vector $\mathbf{r}_{21}$ in the detector plane, $J_n(\rho)$ is the Bessel function of the first kind of integer order n, and the integration is performed over the area of a particle. According to the structure of I_{q,ψ_0}^n, its value strongly depends on the symmetry of a particle.

The intensity $I_{\psi_k}(q, \varphi)$ scattered from a particle in an arbitrary orientation ψ_k is related to the intensity $I_{\psi_0}(q, \varphi)$ scattered from a particle in the reference orientation ψ_0 (we assume in the following without loss of generality that $\psi_0 = 0$) as $I_{\psi_k}(q, \varphi) = I_{\psi_0}(q, \varphi - \psi_k)$. Applying the shift theorem for the Fourier transforms [55], we obtain for the corresponding Fourier components of the intensities, $I_{q,\psi_k}^n = I_{q,\psi_0}^n \exp(-in\psi_k)$. Using these relations, for a dilute 2D system of identical particles, we can write for the Fourier components I_q^n of the intensity $I(q, \varphi)$ scattered from N particles (Eq. 5)

$$I_q^n = I_{q,\psi_0}^n \sum_{k=1}^{N} e^{-in\psi_k} = I_{q,\psi_0}^n \mathbf{A}_n, \tag{9}$$

where $\mathbf{A}_n = \sum_{k=1}^{N} \exp(-in\psi_k)$ is a random phasor sum [56]. Equation (9) leads to the following expression for the small-angle X-ray scattering (SAXS) intensity, $\langle I(q, \varphi) \rangle_\varphi = N I_{q,\psi_0}^0$.

2. Dense Systems

In the case of a dense system, when the average distance between particles is of the order of the size of a single cluster, the Fourier components I_q^n of the intensity $I(\mathbf{q})$ (Eq. 4) can contain a substantial interparticle contribution.

In this case, I_q^n can be presented as a sum of two terms as follows:

$$I_q^n = I_{sp}^n(q) + I_{ip}^n(q). \tag{10}$$

Here $I_{sp}^n(q)$ is attributed to a single-particle structure discussed before, and $I_{ip}^n(q)$ is defined by the interparticle correlations [12, 13, 16]. In a 2D system, these two terms are [12, 13, 16]

$$I_{sp}^n(q) = I_{q,\psi_0}^n \mathbf{A}_n, \tag{11a}$$

$$I_{ip}^n(q) = 2 \sum_{k_2 > k_1} \int \int \widetilde{\rho}_{k_1}^*(\mathbf{r}_1)\widetilde{\rho}_{k_2}(\mathbf{r}_2)J_n(q|\mathbf{R}_{k_2,k_1}^{21}|)e^{-in\phi_{\mathbf{R}_{k_2,k_1}^{21}}} d\mathbf{r}_1 d\mathbf{r}_2, \tag{11b}$$

where $\phi_{\mathbf{R}_{k_2,k_1}^{21}}$ is the angle of the vector $\mathbf{R}_{k_2,k_1}^{21}$ in the sample plane.

C.   3D Disordered Systems

Here, we consider a general case of 3D systems in which one or more particles are distributed with random positions and orientations in 3D space. In the case of 3D systems nonzero odd Fourier components can be also present when scattering to high angles is considered, due to the effects of Ewald sphere curvature.

In general, the scattering vector $\mathbf{q} = (\mathbf{q}^\perp, q^z)$ can be decomposed into two components: (1) $\mathbf{q}^\perp$ that is perpendicular and (2) q^z that is parallel to the direction of the incident beam (see Fig. 3b). We also define the perpendicular $\mathbf{R}_{k_2,k_1}^{\perp 21} = \mathbf{R}_{k_2,k_1}^\perp + \mathbf{r}_{21}^\perp$, and the z-components $Z_{k_2,k_1}^{21} = Z_{k_2,k_1} + z_{21}$ of the radius vectors (see Figs. 2a and 3). Using these notations we can write Eq. (4) in the following form:

$$I(\mathbf{q}) = \sum_{k_1,k_2=1}^{N} e^{-iq^z \cdot Z_{k_2,k_1}} \int \int \widetilde{\rho}_{k_1}^*(\mathbf{r}_1^\perp, q^z)\widetilde{\rho}_{k_2}(\mathbf{r}_2^\perp, q^z)e^{i\mathbf{q}^\perp \cdot \mathbf{R}_{k_2,k_1}^{\perp 21}} d\mathbf{r}_1^\perp d\mathbf{r}_2^\perp. \tag{12}$$

Here, we introduced a modified complex valued electron density function, defined as follows:

$$\widetilde{\rho}_{k_i}(\mathbf{r}_i^\perp, q^z) = \int \rho_{k_i}(\mathbf{r}_i^\perp, z)e^{-iq^z z}dz. \tag{13}$$

In the case of wide-angle scattering, the effect of the Ewald sphere curvature (see Fig. 3b), which manifests itself by the presence of the exponential factors $e^{-iq^z \cdot Z_{k_2,k_1}}$ and $e^{-iq^z z}$ in Eqs. (12) and (13), may become important. This effect can break the scattering symmetry of a diffraction pattern, characteristic for the scattering on a positive valued electron density (Friedel's law) and may help to reveal symmetries that cannot be directly observed in the small-angle scattering case. A wide-angle scattering geometry may become important for scattering on atomic systems with local interatomic distances of the order of few Ångstroms.

For simplicity, we will consider here a 3D system consisting of particles composed of isotropical identical scatterers. The modified electron density

of a particle according to Eq. (13) can be represented in the following form [7]:

$$\widetilde{\rho}_k(\mathbf{r}^\perp, q^z) = f(q) \sum_{i=1}^{N_s} \delta(\mathbf{r}^\perp - \mathbf{r}_i^\perp) e^{-iq^z z_i}. \tag{14}$$

Here $f(q)$ is a form-factor of a scatterer, and N_s is a number of scatterers in the cluster. The coordinates $(\mathbf{r}_i^\perp, z_i)$ define the position of the i-th scatterer inside the k-th cluster. Using this definition and performing Fourier transformation of Eq. (12), we obtain for the Fourier coefficients of intensity [12, 13]

$$I^n(q^\perp, q^z) = (i)^n |f(q)|^2 \sum_{k_1,k_2=1}^{N} \sum_{l,m=1}^{N_s} e^{-iq^z Z_{k_2,k_1}^{ml}} J_n(|\mathbf{q}^\perp| \cdot |\mathbf{R}_{k_2,k_1}^{\perp ml}|) e^{-in\phi_{\mathbf{R}_{k_2,k_1}^{\perp ml}}}, \tag{15}$$

where the summation over index l is performed over the positions of scatterers in the cluster k_1, and the summation over index m is performed over the positions of scatterers in the cluster k_2. We note here that due to the property of the Bessel functions $[J_n(0) = 0$ for $n \neq 0]$, the terms with $k_1 = k_2$ and $l = m$ are equal to zero. Taking into account that the terms with interchanged indices, that is, k_1, k_2 and k_2, k_1, as well as l, m and m, l, differ from each other by a change of the sign of Z_{k_2,k_1}^{ml} and by an additional factor $(-1)^n$, which arises due to the change of the phase $\phi_{\mathbf{R}_{k_2,k_1}^{\perp ml}} = \phi_{\mathbf{R}_{k_1,k_2}^{\perp lm}} + \pi$, we have the following for *even* values of n in Eq. (15) [12, 13]:

$$I^n(q^\perp, q^z)$$

$$= 2(i)^n |f(q)|^2 \left[\sum_{\substack{1\leq k_1 \leq N \\ k_1 < k_2 \leq N}} \sum_{\substack{1\leq l\leq N_s \\ 1\leq m\leq N_s}} \cos(q^z Z_{k_2,k_1}^{ml}) J_n(|\mathbf{q}^\perp| \cdot |\mathbf{R}_{k_2,k_1}^{\perp ml}|) e^{-in\phi_{\mathbf{R}_{k_2,k_1}^{\perp ml}}} \right.$$

$$\left. + \sum_{1\leq k\leq N} \sum_{\substack{1\leq l\leq N_s \\ l\leq m\leq N_s}} \cos(q^z Z_k^{ml}) J_n(|\mathbf{q}^\perp| \cdot |\mathbf{R}_k^{\perp ml}|) e^{-in\phi_{\mathbf{R}_k^{\perp ml}}} \right]. \tag{16}$$

For *odd* values of n,
$$I^n(q^\perp, q^z)$$

$$= -2(i)^{n+1} |f(q)|^2 \left[\sum_{\substack{1\leq k_1 \leq N \\ k_1 < k_2 \leq N}} \sum_{\substack{1\leq l\leq N_s \\ 1\leq m\leq N_s}} \sin(q^z Z_{k_2,k_1}^{ml}) J_n(|\mathbf{q}^\perp| \cdot |\mathbf{R}_{k_2,k_1}^{\perp ml}|) e^{-in\phi_{\mathbf{R}_{k_2,k_1}^{\perp ml}}} \right.$$

$$\left. + \sum_{1\leq k\leq N} \sum_{\substack{1\leq l\leq N_s \\ l\leq m\leq N_s}} \sin(q^z Z_k^{ml}) J_n(|\mathbf{q}^\perp| \cdot |\mathbf{R}_k^{\perp ml}|) e^{-in\phi_{\mathbf{R}_k^{\perp ml}}} \right], \tag{17}$$

where $\mathbf{R}_k^{\perp ml} = \mathbf{R}_{k,k}^{\perp ml}$ and $Z_k^{ml} = Z_{k,k}^{ml}$. From the performed analysis, we can see that, due to the curvature of the Ewald sphere (nonzero q^z component), we obtain nonzero odd Fourier components of the CCF when scattering from a 3D system. These components become negligibly small for experimental conditions corresponding to a flat Ewald sphere, considered in Section II.B.

In the case of a dilute sample, the Fourier components of intensity defined in Eq. (14) reduce to

$$I^n(q^\perp, q^z) = (i)^n |f(q)|^2 \sum_{k=1}^{N} \sum_{l,m=1}^{N_s} e^{-iq^z z_k^{ml}} J_n(|\mathbf{q}^\perp| \cdot |\mathbf{r}_k^{\perp ml}|) e^{-in\phi_{\mathbf{r}_k^{\perp ml}}}. \quad (18)$$

Here, we would like to note that if in a 3D system all particles are aligned (as in Fig. 1b) or rotated around a single axis parallel to the incoming beam (Fig. 1c), and conditions of small-angle scattering are satisfied ($q_z \simeq 0$), then the analysis of scattering can be performed in the same way as for a 2D system described in Section II.B.

D.   Two- and Three-Point Angular CCFs and Their Fourier Decomposition

1.   General Definitions

The two-point CCF defined for a single realization of a disordered system at two resolution rings, q_1 and q_2, is given by [3, 12, 13, 57] (see Fig. 3c)

$$C(q_1, q_2, \Delta) = \left\langle \widetilde{I}(q_1, \varphi) \widetilde{I}(q_2, \varphi + \Delta) \right\rangle_\varphi, \quad (19)$$

where $0 \leq \Delta \leq 2\pi$ is the angular coordinate, $\widetilde{I}(q, \varphi) = I(q, \varphi) - \langle I(q, \varphi) \rangle_\varphi$ is the intensity fluctuation function, and $\langle f(\varphi) \rangle_\varphi = (1/2\pi) \int_0^{2\pi} f(\varphi) d\varphi$ denotes the average over the angle φ. We should note here that due to fluctuations of intensity on a pulsed sources as XFELs, the normalized intensity should be used in Eq. (19). In practice, we used normalization to the integrated intensity measured on the detector from each pulse.

In a similar way, the three-point CCF for a single realization of a system is defined at three resolution rings, q_1, q_2, and q_3, as [3, 18] (see Fig. 3d) as follows:

$$C(q_1, q_2, q_3, \Delta_1, \Delta_2) = \left\langle \widetilde{I}(q_1, \varphi) \widetilde{I}(q_2, \varphi + \Delta_1) \widetilde{I}(q_3, \varphi + \Delta_2) \right\rangle_\varphi. \quad (20)$$

Here $0 \leq \Delta_1 \leq 2\pi$ and $0 \leq \Delta_2 \leq 2\pi$ are the angular coordinates.

It is convenient to analyze CCFs using a Fourier series decomposition in the $(0, 2\pi)$ interval [12, 13]. In the case of the two-point CCF $C(q_1, q_2, \Delta)$, it gives

$$C(q_1, q_2, \Delta) = \sum_{n=-\infty}^{\infty} C_{q_1,q_2}^n e^{in\Delta}, \tag{21a}$$

$$C_{q_1,q_2}^n = \frac{1}{2\pi} \int_0^{2\pi} C(q_1, q_2, \Delta) e^{-in\Delta} d\Delta. \tag{21b}$$

Here, C_{q_1,q_2}^n is the n-th component in the Fourier series expansion of $C(q_1, q_2, \Delta)$, and $C_{q_1,q_2}^0 = 0$ at $n = 0$ by definition (see Eq. 19). Substituting Eq. (19) into Eq. (21b) and applying the Fourier convolution theorem, we get the following:

$$C_{q_1,q_2}^n = I_{q_1}^{n*} \cdot I_{q_2}^n. \tag{22}$$

Here, I_q^n are the components of the Fourier expansion of the scattered intensity $I(q, \varphi)$ defined in (6b). As soon as $I_q^{-n} = I_q^{n*}$, we obtain for the Fourier components of CCFs and $C_{q_1,q_2}^{-n} = C_{q_1,q_2}^{n*}$.

In the specific case, when $q_1 = q_2 = q$, Eqs. (21a) and (22) reduce to

$$C(q, \Delta) = 2 \sum_{n=1}^{\infty} C_q^n \cos(n\Delta), \tag{23a}$$

$$C_q^n = |I_q^n|^2, \quad C_q^n \geq 0. \tag{23b}$$

According to (23a), a strong single cosine dependence of $C(q, \Delta)$ can be observed for those values of q, at which one of the Fourier components C_q^n significantly dominates over all others [11]. Such components can be related to the structure and symmetry of the system [12, 13, 16].

The Fourier series expansion of the three-point CCF $C(q_1, q_2, q_3, \Delta_1, \Delta_2)$ can be written as follows:

$$C(q_1, q_2, q_3, \Delta_1, \Delta_2) = \sum_{n_1=-\infty}^{\infty} \sum_{n_2=-\infty}^{\infty} C_{q_1,q_2,q_3}^{n_1,n_2} e^{in_1\Delta_1} e^{in_2\Delta_2}, \tag{24a}$$

$$C_{q_1,q_2,q_3}^{n_1,n_2} = \left(\frac{1}{2\pi}\right)^2 \int_0^{2\pi} \int_0^{2\pi} C(q_1, q_2, q_3, \Delta_1, \Delta_2) e^{-in_1\Delta_1} e^{-in_2\Delta_2} d\Delta_1 d\Delta_2. \tag{24b}$$

Here $C_{q_1,q_2,q_3}^{n_1,n_2}$ are the Fourier components of the three-point CCF, and $C_{q_1,q_2,q_3}^{n_1,n_2} = 0$ for $n_1 = 0$, $n_2 = 0$, and $n_1 = -n_2$. Substituting Eq. (20) into Eq. (24b), one can get the following [18]:

$$C_{q_1,q_2,q_3}^{n_1,n_2} = I_{q_1}^{(n_1+n_2)*} I_{q_2}^{n_1} I_{q_3}^{n_2}. \tag{25}$$

In general, Eq. (25) determines a relation between three different Fourier components of intensity I_q^n of the order n_1, n_2 and $n_1 + n_2$, defined on three resolution rings, q_1, q_2, and q_3.

In practical applications, one would need to consider CCFs and Fourier components of CCFs averaged over a sufficiently large number M of diffraction patterns [16, 18]. Such averaging can be defined as a general rule

$$\langle C \rangle_M = 1/M \sum_{m=1}^{M} C_m, \tag{26}$$

where C is one of the quantities $C(q_1, q_2, \Delta)$, $C(q_1, q_2, q_3, \Delta_1, \Delta_2)$, C_{q_1,q_2}^n, or $C_{q_1,q_2,q_3}^{n_1,n_2}$ and C_m is defined for the m-th realization of a disordered system.

The analysis presented here shows that in the Fourier domain, the two-point angular intensity CCF reduces to a product of two Fourier components of intensity (see Eq. 22). Similarly in the case of the three-point CCF, we obtain a product of three Fourier components of intensity (see Eq. 25). Taking into account that intensity distribution itself gives information on density–density (or pair correlation) functions, it means that the angular XCCA may be considered as a particular case of the higher order correlation functions [12, 13]. However, the general question of revealing the higher order correlation functions of an arbitrary form in disordered systems [58] by means of cross-correlation approaches remains open.

2.   *Analysis of Disordered Systems by Angular CCFs*

Substituting Eq. (9) in Eq. (22) in the limit of dilute systems, we have for the Fourier components C_{q_1,q_2}^n of the CCF the following expression:

$$C_{q_1,q_2}^n = I_{q_1,\psi_0}^{n*} I_{q_2,\psi_0}^n |\mathbf{A}_n|^2. \tag{27}$$

The statistical behavior of $\mathbf{A}_n$ has been analyzed for different angular distributions of orientations of particles in the system (see Refs. 12, 13 and 16). It is clear that in the case of a completely oriented system of particles (all $\psi_k = 0$), the square amplitude of the random phasor sum $|\mathbf{A}_n|^2$ is equal to N and $C_{q_1,q_2}^n = N I_{q_1,\psi_0}^{n*} I_{q_2,\psi_0}^n$. In the case of a uniform distribution of orientations of particles, $|\mathbf{A}_n|^2$ fluctuates around its mean value $\langle |\mathbf{A}_n|^2 \rangle_M = N$ with the standard deviation $\sigma_{|\mathbf{A}_n|^2} = N$. Averaging the Fourier components C_{q_1,q_2}^n over a large number M of diffraction patterns leads to the following asymptotic result: [12, 13, 16]

$$\left\langle C_{q_1,q_2}^n \right\rangle_M = I_{q_1,\psi_0}^{n*} I_{q_2,\psi_0}^n \cdot \left\langle |\mathbf{A}_n|^2 \right\rangle_M \xrightarrow[M \to \infty]{} N I_{q_1,\psi_0}^{n*} I_{q_2,\psi_0}^n. \tag{28}$$

Here $\langle \cdots \rangle_M$ denotes statistical averaging over M diffraction patterns. Importantly, the ensemble-averaged Fourier components $\langle C_{q_1,q_2}^n \rangle_M$ converge to a scaled product of the two Fourier components of intensity I_{q_1,ψ_0}^{n*} and I_{q_2,ψ_0}^n associated with a single particle.

Using the approach developed before, it is possible to determine the amplitudes $|I_{q,\psi_0}^n|$ and phases ϕ_{q,ψ_0}^n (for $n \neq 0$) of the Fourier components

$I^n_{q,\psi_0} = |I^n_{q,\psi_0}| \exp(i\phi^n_{q,\psi_0})$ associated with a single particle. They can be obtained using Eq. (28) [18]. This equation gives the phase difference between two Fourier components $I^n_{q_1,\psi_0}$ and $I^n_{q_2,\psi_0}$ of the same order n, defined at two different resolution rings, q_1 and q_2,

$$\arg\left[\left\langle C^n_{q_1,q_2}\right\rangle_M\right] = \phi^n_{q_2,\psi_0} - \phi^n_{q_1,\psi_0}. \tag{29}$$

Similar to the Fourier components of the two-point CCF, the Fourier components of the three-point CCF equation (25) can be expressed in the limit of a dilute system as follows: [18]

$$C^{n_1,n_2}_{q_1,q_2,q_3} = I^{(n_1+n_2)*}_{q_1,\psi_0} I^{n_1}_{q_2,\psi_0} I^{n_2}_{q_3,\psi_0} \cdot \mathbf{A}_{n_1,n_2}, \tag{30}$$

Here $\mathbf{A}_{n_1,n_2} = \sum^N_{i,j,k=1} \exp\{i[(n_1 + n_2)\psi_i - n_1\psi_j - n_2\psi_k]\}$ is another random phasor sum. Our analysis shows [18] that in the case of a uniform distribution of orientations of N particles, the statistical average $\langle\mathbf{A}_{n_1,n_2}\rangle_M$ converges to N for a sufficiently large number M of diffraction patterns,

$$\left\langle C^{n_1,n_2}_{q_1,q_2,q_3}\right\rangle_M \xrightarrow[M\to\infty]{} N I^{(n_1+n_2)*}_{q_1,\psi_0} I^{n_1}_{q_2,\psi_0} I^{n_2}_{q_3,\psi_0}. \tag{31}$$

An important result of Eq. (31) is that the ensemble-averaged Fourier components $\langle C^{n_1,n_2}_{q_1,q_2,q_3}\rangle_M$ converge to a scaled product of three Fourier components of intensity $I^{(n_1+n_2)*}_{q_1,\psi_0}$, $I^{n_1}_{q_2,\psi_0}$, and $I^{n_2}_{q_3,\psi_0}$ associated with a single particle. Equation (31) also provides the following phase relation:

$$\arg\left[\left\langle C^{n_1,n_2}_{q_1,q_2,q_3}\right\rangle_M\right] = \phi^{n_1}_{q_2,\psi_0} + \phi^{n_2}_{q_3,\psi_0} - \phi^{(n_1+n_2)}_{q_1,\psi_0}. \tag{32}$$

This equation determines the phase difference between three Fourier components $I^{(n_1+n_2)}_{q_1,\psi_0}$, $I^{n_1}_{q_2,\psi_0}$, and $I^{n_2}_{q_3,\psi_0}$ of different order n defined on three resolution rings. If $n_1 = n_2 = n$ and $n_3 = 2n$, Eq. (32) reduces to a particular form, giving the phase relation between Fourier components of only two different orders, n and $2n$. Phase relations (29) and (32) can be used to determine the phases of the complex Fourier components I^n_{q,ψ_0} using measured CCFs from a disordered system of particles [18, 26].

The influence of interparticle correlations on CCFs in dense systems were discussed in detail in Refs. 12 and 16.

III.   APPLICATIONS

In this section, we review the applications of the CCFs in X-ray studies of materials divided into two major groups. The first part of applications is related to the problem of a single-particle structure recovery in the fluctuation X-ray scattering (FXS) experiments [3, 14, 17, 18, 21, 24, 26, 46, 50, 57, 59–63]. The second part is related to the studies of structural properties of disordered and partially

ordered systems, such as colloids, metallic glasses, liquid crystals, and polymers. Applications, where CCFs serve as subsidiary mathematical tools and are not directly related to the analysis of material properties, for example, in diffraction pattern classification algorithms [64], or powder diffraction analysis software [65], will not be discussed here. While concentrating mostly on X-ray applications, in particular cases we also refer to the results obtained in electron or light scattering experiments, both to highlight the generality of the cross-correlation approaches and their peculiarities for different techniques.

A. Single-Particle Structure Recovery from FXS

With the emergence of XFELs [8–10], single-particle diffractive imaging experiments became one of the important challenges of materials research [66–68]. The basic idea behind a single-particle experiment is to determine the structure of particles (e.g., macromolecules and viruses) that cannot be crystallized and studied by conventional scattering techniques. While it is expected that using the high-power ultrashort coherent pulses produced by XFELs, the structure of a single particle can be measured before its desintegration by intense radiation [69–73], the practical realization of this idea is still challenging. Complementary techniques that could profit out of the unique properties of XFELs and provide structural information on a single particle have become of great interest.

One of the potential approaches that could resolve this problem is based on the paradigm "scatter from many — determine single" [46], which is directly related to the FXS experiment proposed by Kam [3]. In such an experiment, a limited number of identical particles N in solution is illuminated by the X-ray beam, with the exposure time shorter than the rotational diffusion time of the particles [3]. At the time this experiment was proposed, FXS measurements would ideally require a frozen dilute solution of particles to slow down particle dynamics [59]. Nowadays, this requirement can be realized at modern XFELs, where the sample looks "frozen" to an incident X-ray pulse of femtosecond duration. Such experiment would allow to measure the instantaneous fluctuations of the scattered intensity about the average signal, and to use this information for structure recovery [3, 49, 50, 59]. The advantage of the FXS experiment is that the scattered intensity is N times higher as compared to a single-particle scattering experiment, that is especially attractive for weakly scattering biological particles. Another important advantage is that the particles do not need to be crystallized, as it is required in conventional crystallographic techniques, or modern serial nanocrystallography experiments [74, 75].

Although the problem of single-particle structure determination from FXS is, in general, related to recovery of a 3D structure of a particle, we start with a particular case of 2D structure determination. Here, the term "2D structure" refers to a projection of the electron density of a particle on a certain plain, while "3D structure" means full structure of a particle in 3D space.

Recovery of a single-particle structure from the measured FXS data can be done in various ways. According to one of the approaches, the real-space structure of a particle can be determined in two steps [15, 18, 24–26, 52, 57, 60, 76]. On the first step, the intensity distribution corresponding to a single particle is recovered from the FXS data using the CCFs. On the second step, the determined intensity distribution in reciprocal space is used to recover the real-space structure of a single particle by means of the iterative phase retrieval algorithms [77–80], like in conventional coherent X-ray diffractive imaging (CXDI). Another approach is based on direct fitting of the real-space structure to the measured X-ray data using CCFs as constraints [17, 62]. It might be also possible to reconstruct the intensity distribution in reciprocal space and the real-space structure concurrently [14]. Significant advance in this direction was accomplished recently on the basis of a multitiered iterative phasing algorithm [21]. Depending on dimensionality of the problem and symmetry of the system, cross-correlation methods operate with different basis functions to expand the electron density of a particle, the scattered intensity, and the CCFs. A convenient choice for 2D structures is the circular harmonics expansion [18, 24, 26, 57, 60, 76], while spherical harmonics [3, 25, 34, 48–52], icosahedral harmonics [15], and 3D Zernike polynomials [17, 53] are used in the case of 3D structures.

1. 2D Structure Determination

We consider the problem of 2D structure determination of a particle starting from a 2D version of the FXS experiment, where reproducible particles in identical projections are distributed on a 2D plane (e.g., on a substrate), rather than in 3D volume. A finite number of particles N is illuminated by a short X-ray pulse, and particles have random positions and orientations in 2D plane in each realization of the system. The signal-to-noise ratio for the measured correlated signal in such an experiment is independent of the number of particles N and is proportional to $\sqrt{M}$, where M is the number of the measured realizations of a disordered system [3, 16, 81, 82]. Therefore, a large number M of diffraction patterns have to be measured to obtain statistically converging values of the CCFs [3, 18, 24, 26, 57, 60, 76]. The requirement of the finite number of particles in the beam is dictated by the fact that the average scattered intensity scales proportionally to N, while the spatial intensity fluctuations are proportional to $\sqrt{N}$ [3, 16, 18, 83]. This, together with the technical capabilities of a typical experimental setup, sets the upper limit on the actual number of particles that can be simultaneously present in the beam. Theoretically, this number can be comparably large for an ideal noise-free detector with an infinite dynamic range. However, due to different sources of the background signal, for example, scattering contribution from a solvent, interparticle interference terms, and incident intensity fluctuations as well as other experimental factors, this number is finite [16]. In practice, it should be determined as a compromise between the scattered signal and FXS contrast.
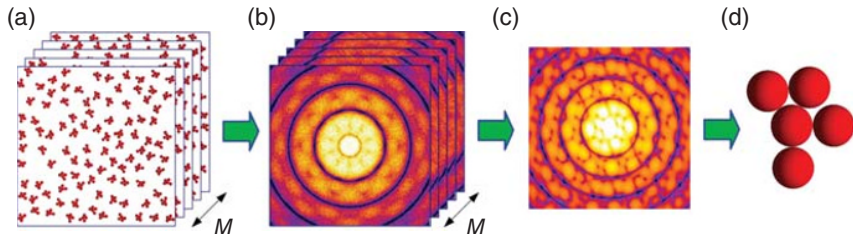
Figure 4. A concept of recovery of the structure of a single particle using X-ray scattering data from many particles. A large number M of realizations of a disordered system (a) composed of many identical particles is used to collect M diffraction patterns (b). X-ray cross-correlation analysis is applied to this X-ray dataset to recover a diffraction pattern (c) corresponding to a single particle. The structure of a single particle (d) is determined applying phase retrieval algorithms to the recovered diffraction pattern (c). Reproduced from Ref. 46. Used under CC By 3.0, http://creativecommons.org/licenses/by/3.0/. (*See insert for color representation of the figure.*)

A direct method for 2D structure recovery from FXS has been recently proposed in Ref. 18. It allows *ab initio* structure recovery without any *a priori* knowledge about a particle, and consist of few steps illustrated in Fig. 4. The great advantage of this method is that the recovery of the diffraction pattern corresponding to a single particle (Fig. 4c) from the measured X-ray dataset (Fig. 4b) can be done directly, without model assumptions or fitting. This is achieved by using algebraic formalism of ensemble-averaged two-point $\langle C(q_1, q_2, \Delta)\rangle_M$ and three-point $\langle C(q_1, q_2, q_3, \Delta_1, \Delta_2)\rangle_M$ CCFs (see Eqs. 19 and 20) and their respective Fourier components (Eqs. 28 and 31). The key point here is that only the CCFs determined at $q_1 \neq q_2 \neq q_3$ are used in the analysis [18]. This allows to minimize undesired scattering contributions from the interparticle interference and obtain simple relations between the Fourier components as they appear in Eqs. (28) and (31). It is also worth mentioning that Eqs. (28) and (31) contain redundant information that can be used to cross-check the obtained solutions. One limiting factor with this approach can be sufficient signal to reliably record the three-point CCFs $\langle C(q_1, q_2, q_3, \Delta_1, \Delta_2)\rangle_M$.

The recovered diffraction pattern corresponding to a single particle (Fig. 4c) can be further analyzed by applying iterative phase retrieval algorithms to reconstruct the 2D electron density of a particle. The results of application of this method to simulated x-ray data (see for details Ref. 18) are illustrated in Fig. 5. The 2D structure of two objects, a cluster with five-fold rotational symmetry (Fig. 5g) and an asymmetric cluster (Fig. 5h), was successfully reconstructed by applying a combination of hybrid input-output (HIO) and error reduction (ER) algorithms to the recovered diffraction patterns (Fig. 5e and f, respectively).

A similar approach has been experimentally applied to a 2D system of reproducible particles [26]. In this X-ray scattering experiment, gold nanostructures of about 300 nm in size were randomly distributed on a Si_3N_4 membrane, with the
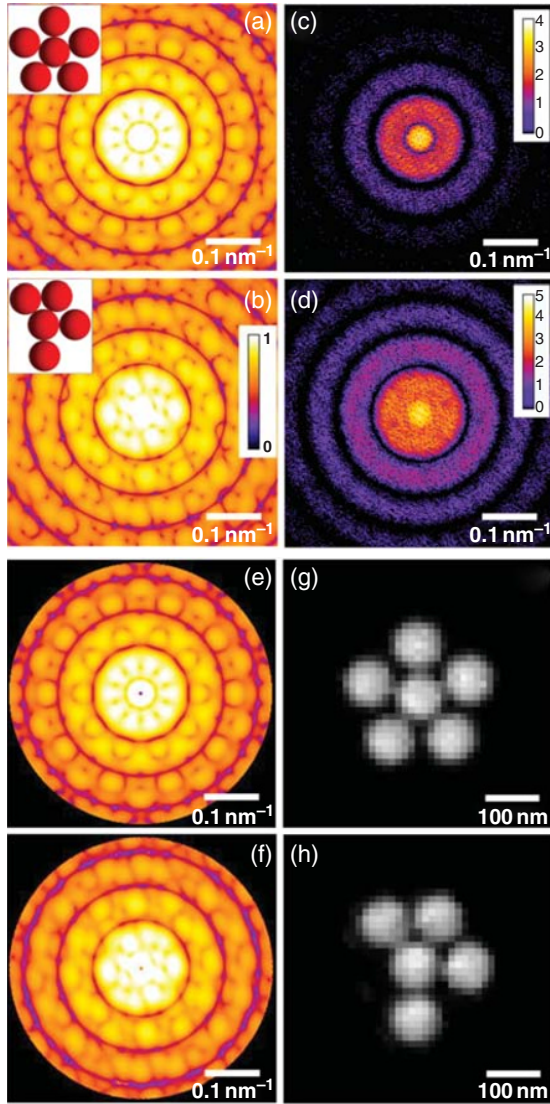
Figure 5. (a and b) Scattered intensity (logarithmic scale) calculated for a single pentagonal cluster (a) and an asymmetric cluster (b) (clusters are shown in the insets). (c and d) Coherently scattered intensity from a disordered system consisting of $N = 10$ clusters in random position and orientation with the incident fluence of 10^{12} and 10^{13} photons/25 μm^2 for pentagonal and asymmetric clusters, respectively. (e and f) Scattered intensity corresponding to a single pentagonal (e) and asymmetric (f) clusters recovered from $M = 10^5$ diffraction patterns of the form (c) and (d), correspondingly. (g and h) Structure of a single cluster reconstructed by an iterative phase retrieval algorithm using the diffraction patterns shown in (e) and (f). The intensity in (a), (b), (e), and (f) is given in arbitrary units, and in (c) and (d) in photon counts. Reproduced from Ref. [18] open access. (*See insert for color representation of the figure.*)

threefold rotational axis aligned perpendicular to the substrate (Fig. 6). Samples of different densities were measured, with the average number of particles $N \approx$ 2.5/20/80 in the X-ray beam. A comparison of the recovered structure of a single particle (see Fig. 6c) with the scanning electron microscope (SEM) image (Fig. 6e) demonstrates the potential of the proposed approach.

Another approach for 2D structure recovery based on the circular harmonics expansion of two- and three-point CCFs was proposed by Saldin et al. [57]. While the two-point CCF $C(q_1, q_2, \Delta)$ used in Ref. [57] leads to the same relation between the Fourier components as in Eq. (28), the three-point CCF was defined on the same momentum transfer ring q as $C(q, q, \Delta) = \langle (I(q, \varphi)^2 I(q, \varphi + \Delta) \rangle_\varphi$. Such definition of the CCF leads to the following relation for the Fourier components: $\langle C_{q,q}^n \rangle_M = N I_q^{n*} \sum_{m \neq 0, n} I_q^m I_q^{n-m}$. This approach does not allow to directly determine the complex coefficients I_q^n without additional constraints. To overcome these difficulties, the authors of Ref. [57] fitted the phases of I_q^n by applying
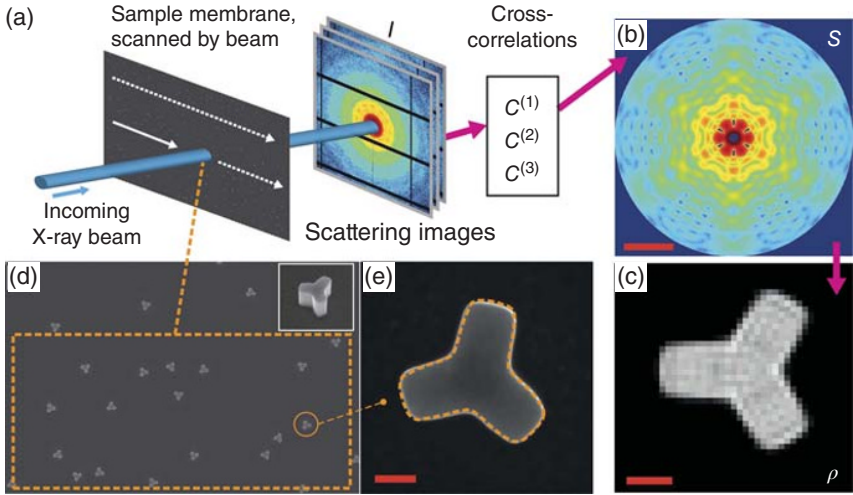
Figure 6. Overview of the cross-correlation-based method applied to the 2D structure determination. The flow of the protocol follows the magenta arrows: (a) the membrane carrying the gold nanostructures is scanned by the X-ray beam, and a number of scattering images are acquired at different positions. The CCFs (C(1), C(2), and C(3)) are calculated as averages over all images, and (b) the single-particle diffraction pattern S is computed. The red bar represents a reciprocal space momentum transfer of 0.1 nm^{-1}. (c) The 2D electron density ρ is finally reconstructed using a phasing algorithm. The red bar corresponds to 100 nm. (d) SEM image of a small part of the sample membrane, showing the particles in random orientations. The dashed orange rectangle covers an area of 14×6 μm^2, which corresponds approximately to the X-ray beam illumination area. (e) Top SEM view of a single particle, on which the dashed orange contour of the reconstructed shape is superimposed. Pedrini et al. [26]. Reproduced with permission of Nature Publishing Group.

simulated annealing algorithm, with additional constraint of mirror line symmetry of the diffraction pattern. One more problem of such definition of the three-point CCF comes from the fact that it suffers from the undesirable contribution of the interparticle scattering, which is present when intensities are correlated at the same values of q in the case of coherent scattering [12, 13, 16, 18, 20, 26].

Meanwhile, few other approaches were proposed for 2D structure recovery based on fitting the phases of the Fourier components I_q^n by means of iterative charge-flipping algorithm [84], and certain constraints on the symmetry of a diffraction pattern [60] or an object [24]. However, these indirect approaches seem to be hardly competitive with phasing approach outlined by Eqs. (7), (28), and (31), where the recovery of a diffraction pattern of a single particle can be done directly, without additional constraints.

2. 3D Structure Determination

X-ray diffraction from a single particle can be considered as a limiting case of scattering from a dilute solution with the number of particles $N = 1$ in the X-ray beam. It can be often assumed as a simplified version of the problem of 3D structure recovery from FXS [15, 17, 25, 34]. Interestingly, that the problem of orientation determination that arises in conventional single-particle imaging [66, 85], at the first glance, is absent when applying cross-correlation approaches to single-particle diffraction data. In fact, it just transforms to the problem of finding the coefficients (or their phases) of the underlying basis functions, used to expand the electron density of a particle and the scattered intensity. However, such reformulated problem might be easier to solve in some cases, especially in the situations of low scattered intensities typical for scattering from single biological molecules, when the orientation determination for individual diffraction patterns is complicated.

Kam proposed to reconstruct the 3D structure of a single particle by applying the CCFs to the FXS data, to determine the coefficients of the spherical harmonics expansion of the 3D electron density of a particle [3, 48]. The problem formulated in this way cannot be directly solved, and additional constraints are required to determine expansion coefficients. Kam suggested to employ "specific site labeling" in a way analogous to the use of substitution markers in X-ray crystallography to facilitate the structure recovery [3]. Although several experiments have indicated feasibility of FXS measurements [1, 59], limited capabilities of the previously available X-ray sources (fluence, focusing optics, detectors) prevented further experimental development of this approach, till it was recently revisited by several groups [12, 13, 17, 21, 24, 25, 34, 62, 83].

For example, it has been proposed [34] to use the two-point CCFs averaged over diffraction patterns from single particles in different orientations, to recover the scattered intensity distribution of a single particle without determining the relative orientations of the individual diffraction patterns. It was demonstrated that this can

be done by fitting coefficients of the spherical harmonics expansion to the measured CCFs [34]. A limited number of these coefficients can be used to reconstruct the low-resolution 3D shape of a molecule, potentially improving the results that could be obtained from the analysis of SAXS data [86, 87]. Another approach has been used in Ref. [25], where in addition to the experimentally determined two-point CCF, a three-point CCF of the form $C(q_1, q_2, \Delta) = \langle (I(q_1, \varphi)^2 I(q_2, \varphi + \Delta) \rangle_\varphi$ was used to fit the coefficients of the spherical harmonics expansion. The approach was applied to the experimental data measured at LCLS from single polystyrene dimers of about 200 nm in size (see Fig. 7). It was deduced from the measured dataset that the scattered intensity distribution has cylindrical symmetry, and this fact was used to reduce the problem of determination of the expansion coefficients to the problem of finding their signs. The recovered intensity distribution of a single dimer was then used in the relaxed averaged alternating reflection (RAAR) algorithm [88] to reconstruct the electron density of a single dimer (see Fig. 7d).

Additional knowledge about the symmetry of particles can simplify the problem of the 3D structure recovery from FXS [15, 25, 50, 62]. It was demonstrated by Saldin et al. [15] that if a particle possesses icosahedral symmetry, the icosahedral harmonics expansion of the scattered intensity can be applied instead of the spherical harmonics expansion. In this case, the icosahedral harmonics expansion coefficients appear to be real, and only their signs need to be determined (similar to Ref. [25]), and this was done by fitting the experimentally determined two-point CCFs [15].

As it was already mentioned, in some cross-correlation approaches a real-space particle structure is directly fitted to the measured CCF and SAXS data, without reconstructing the scattered intensity distribution of a particle on the intermediate stage [17, 62]. It has been proposed in Refs. [17, 53] to use the 3D Zernike polynomials as basis functions to expand the 3D electron density of a particle. Starting from a trial voxelized representation of the protein in solution, a reverse Monte Carlo method [89] has been applied to fit the model to the measured two-point CCFs $C(q, \Delta)$ [17]. It was pointed by the authors that the Zernike expansion method can accurately model the holes/cavities of macromolecules, as well as the excluded and surface-bound solvent, which is usually not well handled in the methods based on the spherical harmonics expansion [53]. In some cases, the Zernike expansion method can also be more computationally efficient as compared to spherical harmonics expansion [53]. The applicability of this approach was demonstrated for various model data (lysine-, arginine-, ornithine (LAO)-binding protein; lysozyme; peroxiredoxin; satellite tobacco mosaic virus), and for a preselected X-ray dataset measured at the LCLS from ellipsoidal iron oxide nanoparticles (150–250 nm in size), showing quite good results of 3D structure recovery [17, 53]. A similar reverse Monte Carlo method was applied to the X-ray data measured from platinum-coated gold dumbbell-shaped particles of about 80 nm in length, randomly distributed on a Si_3N_4 substrate [62]. The 3D particle structure was recovered by fitting the real-space particle model to the
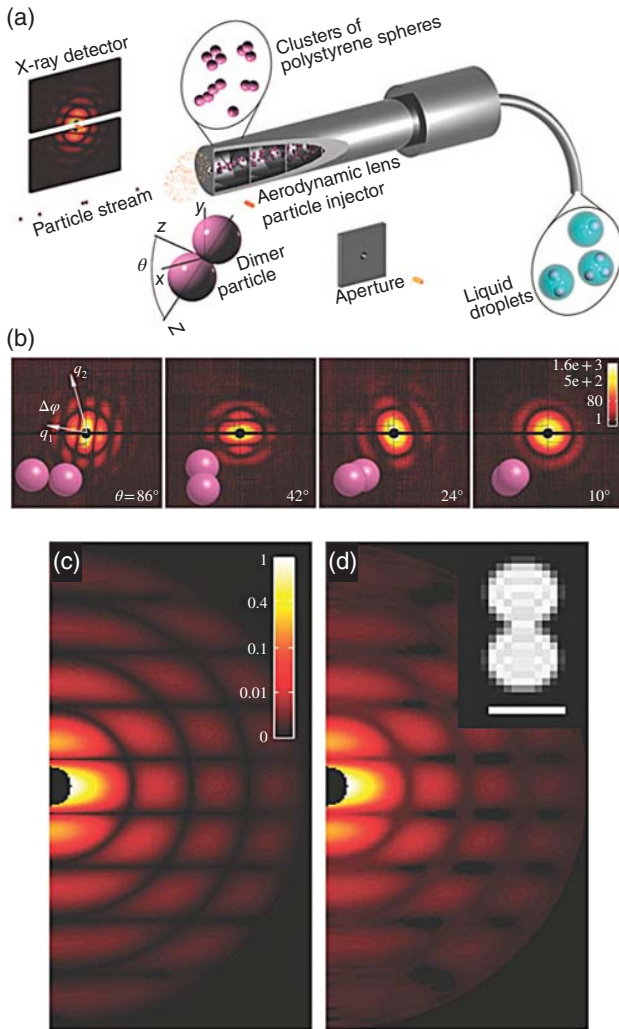
Figure 7. (a) Experimental schematic. Micron-sized droplets emitted from an atmospheric pressure nebulizer contain one or multiple polystyrene spheres. As the droplets transit into the aerodynamic lens stack in a N_2 carrier gas, evaporation leads to single spheres or aerosol-assembled aggregates of random configurations. LCLS X-ray pulses scatter off randomly intersected particles to produce a diffraction pattern recorded on the pnCCD. (b) Experimental diffraction patterns from dimers in several orientations, as indicated in the bottom of each image. The incident X-ray fluence, from left to right, is $(3.7, 2.9, 4.4, 4.0) \times 10^{10}$ photons μm^{-2}. The colour bar indicates detector counts. Projections of the particles on the plane perpendicular to the X-ray beam direction, corresponding to each shot are also shown. (c) Model diffraction pattern from a single dimer. (d) Diffraction pattern from a single dimer obtained from correlation analysis of randomly orientated diffraction patterns. The inset shows the image of azimuthally averaged electron density reconstructed from the experimental pattern. Scale bar is 10 nm. Starodub et al. [25]. Reproduced with permission of Nature Publishing Group. (*See insert for color representation of the figure.*)

measured two-point CCF $C(q, \Delta)$, with the additional assumption of cylindrical symmetry of a particle. Note that the aforementioned reverse Monte Carlo techniques relay on a binary model, where voxels either have a scattering length or do not, and the breakdown of this uniform density approximation in real systems limits the achievable resolution [21].

An interesting though experimentally challenging option for 3D structure recovery was proposed by Elser [14], which could be used in the case of an aligned system of particles. In the proposed model, identical 3D particles are randomly distributed on a 2D plane and are aligned with respect to a single axis. The scattering data are collected at different tilt angles between the plane and the incident beam direction, while particles freely diffuse in angle around their alignment axes. Using the proposed approach, a full 3D intensity distribution of a single particle can be recovered concurrently with the 3D electron density of a particle. This is achieved, particularly, by using circular harmonics expansion of the two-point CCFs. Although this approach was tested only on simulated 2D structures [14], it demonstrated an alternative possibility to solve the FXS problem for aligned systems of 3D particles.

A generalization of the idea of simultaneous reconstruction of the real-space structure and its reciprocal space representation in 3D from FXS data has been recently proposed in Ref. [21]. Iterative recovery of single-particle electron density using multitiered iterative phasing algorithm has been demonstrated. Within this approach, a set of projection operators was proposed, which links the real-space electron density representation and the measured FXS data, employing spherical Henkel and 3D Fourier transform on a polar grid [21]. By iteratively applying these projection operators in ER and HIO algorithms, several model structures were successfully reconstructed. While the reconstructions are characterized by medium resolution, that is 4.8Å for simple geometrical objects, and 6 and 12Å for model proteins with and without a symmetry constraint, correspondingly, the results look encouraging. The proposed approach is quite general and flexible; it can be used with various types of real- and reciprocal space constraints and applied to a different combination of available experimental SAXS and FXS data (also a 2D version of the algorithm is available).

We also would like to briefly comment on another work, which is not directly related to single-particle structure recovery from the FXS data, but employs similar experimental implementation. In this experiment, X-ray scattering from a solution of polydisperse crystalline silver nanoparticles (NPs) with the average size of about 20 nm (see Fig. 8a) was studied using the two-point CCF $C(q_1, q_2, \Delta)$ [28]. Interestingly, despite a very large number of randomly oriented NPs per snapshot, estimated by the authors to be as high as 10^9, they still were able to observe statistically significant correlated scattering signal (Fig. 8b). Such a surprising result, which was also supported by simulations (Fig. 8c), was explained
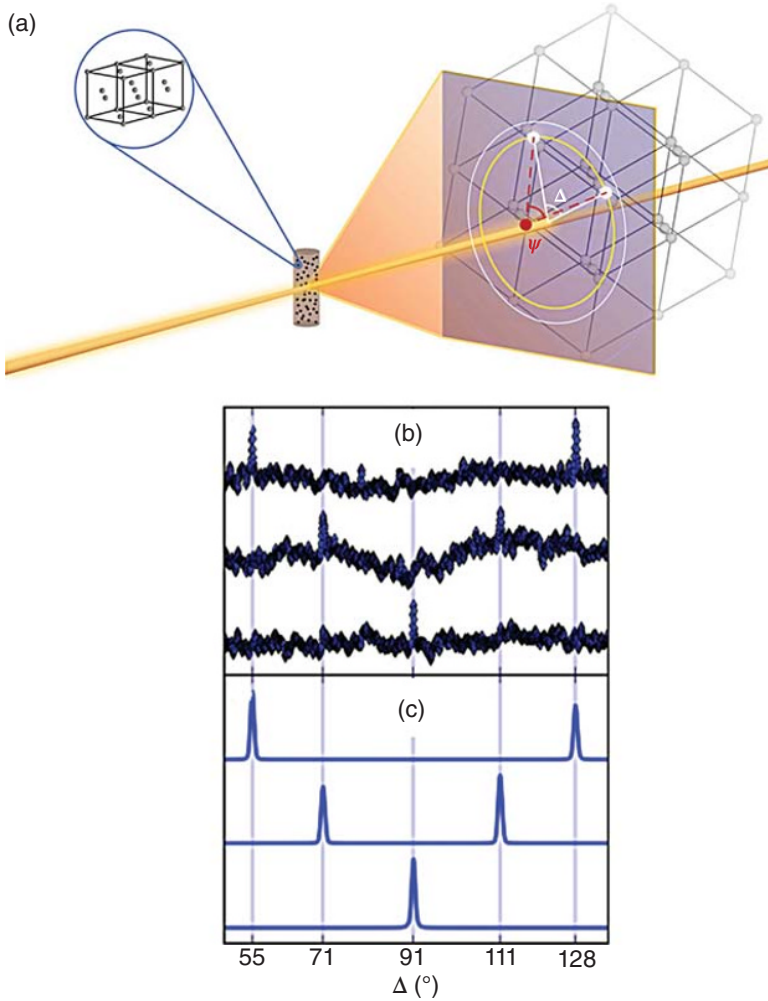
Figure 8. (a) Experimental setup: a kapton capillary filled with a solution of silver NPs (face-centered-cubic). Bragg rings q_{111} and q_{200} are illustrated by circles on the detector plane. At least one of the exposed NPs happens to be oriented such that two reciprocal lattice (body-centered-cubic) peaks are intersecting the detector at q_{111}. Dashed lines represent the scattering vectors (separated by the angle Ψ), and solid lines represent the projection of those vectors onto the detector plane (separated by the angle Δ). (b) From top to bottom, measured correlation functions $C(q_{111}, q_{200}, \Delta)$, $C(q_{111}, q_{111}, \Delta)$, and $C(q_{200}, q_{200}, \Delta)$ from 20 nm silver NPs. (c) Corresponding simulations of the correlations plotted in (b). Vertical lines mark analytical predictions. Reproduced from Ref. 28. Used under CC By 3.0, http://creativecommons.org/licenses/by/3.0/.

by the dominating contribution to the CCF of much smaller number of NPs (of the order 10^3) of a larger size. This experiment demonstrates a possibility to observe correlated X-ray scattering at atomic resolutions, which can be potentially used to apply atomic-scale constraints on particle models with approximately known structure [28].

It is important to note that the problem of FXS is usually considered for a system of *identical (reproducible) particles* having the same structure, which is not always the case in practical applications. The approaches discussed here may tolerate the polydispersity of the particles up to a certain degree [26]. In some cases, it might be possible to study a heterogeneous mixture of different particles, for example, when the molar ratios of the particles in solution are known [90]. More complicated cases of the presence in solution of conformational isomers, impurities, etc, have not been explicitly studied. It has been stressed, that a number of properties of FXS data are inherited from SAXS/WAXS. For instance, it should be possible to distinguish prolate objects from oblates and determine the degree of the structural anisotropy from the Guinier and Porod laws generalized for FXS [63]. Such methods can be used to rapidly characterize samples in a model-free fashion without performing involved structure determination, which is a valuable tool for planning experiments or validating the experimental data.

To summarize, significant methodological and experimental progress has been recently achieved in the recovery of 2D structure of a single particle from FXS data [18, 26]. Nevertheless, it is rather a 3D structure of a particle, and not its 2D projection, that represents great interest for most of the problems in molecular biology, drug design, nanotechnology, or other relevant field of research. The existing approaches for 3D structure recovery from FXS have modest capabilities, since they are largely based on additional constraints or parameter/structure optimization [15, 17, 24, 25, 34, 51–53, 57, 60, 62, 76]. However, the recent extension of the applicability of iterative phasing algorithms to FXS data shows a very promising way toward the solution of the full 3D problem [21]. It was argued that the information contained in two-point CCFs alone is not sufficient for the unique solution of the phase problem that arises in FXS from unoriented 3D structures, and the three-point CCFs are difficult to use in practice [61]. At the same time, it was demonstrated, both in theory and experiment, that for 2D case a combination of two- and three-point CCFs enables a direct reconstruction of single-particle intensity [18, 26]. Recent results also show that reasonable reconstructions of 3D electron density from FXS model structures can be obtained using properly constructed phasing methods and the two-point CCF data only, and the nonuniqueness in reconstruction manifests as small perturbations from the original structure, which decrease with increasing the information content [21]. This brings the hope that further methodological developments in combination with excellent properties of novel X-ray sources would allow *ab initio* 3D structure recovery of a single particle from FXS data.

B.   Correlations in Disordered and Partially Ordered Phases

In this section, we review the applications of CCFs in structural studies of disordered or partially ordered systems. The two-point CCFs have been applied to investigate local structure of colloidal systems [2, 11, 31, 91, 92] and metallic glasses [33], to quantify the BO order in liquid crystals [27, 30], to study structural inhomogeneities in polymers [29, 93], and emerging rotational symmetries in magnetic systems [22, 23].

1.   *Local Structure of Colloidal Systems*

In the light scattering experiment by Clark et al., [2] a two-point CCF with pronounced sixfold modulation has been measured from a single liquid layer of polystyrene spheres of about 230 nm in size. Using two point detectors and a digital cross-correlator, it was possible to directly measure the CCF as a function of angle Δ. The observed form of the CCF was associated with a model of 2D polycrystalline solid with the 2D hexagonal close-packed lattice and large vibrational fluctuations [2]. In a similar light scattering experiment by Pusey et al., much smaller effects in a 3D colloidal liquid were detected [92]. It was pointed out that correlations in the scattered light could be observed, particularly, due to a small scattering volume, comparable with the correlation length in a liquid [2, 91]. This idea was supported later theoretically [94] and further employed in molecular dynamics studies of transient ordering in model quasi-2D liquids [95, 96]. Clark et al. envisaged that the proposed technique of cross-correlation intensity fluctuation spectroscopy can be especially useful in synchrotron X-ray studies of atomic and molecular systems, as soon as the appropriate focusing optics becomes available, satisfying the requirement of sufficiently small illuminated scattering volumes [2, 91].

In the first cross-correlation experiment with X-rays on a colloidal glass [11], the two-point CCF $C(q, \Delta)$ (see Eq. 2) at the same momentum transfer ring $q_1 = q_2 = q$ was measured, showing various types of angular modulations at different values of the momentum transfer q (see Fig. 9). By utilizing a 2D CCD camera, the efficiency of measurements was substantially improved as compared to the multidetector scheme [2]. Recently, X-ray cross-correlation analysis of nanodiffraction data from dried multilayer colloidal films revealed regions with different predominant size of colloidal spheres and different degree of orientational order [31].

2.   *BO Order in Liquid Crystals*

A prominent example of a system with angular correlations is the hexatic phase that combines the properties of both crystals and liquids [42, 97–99]. The so-called bond-orientational order [100] in the hexatic phase can be quantitatively
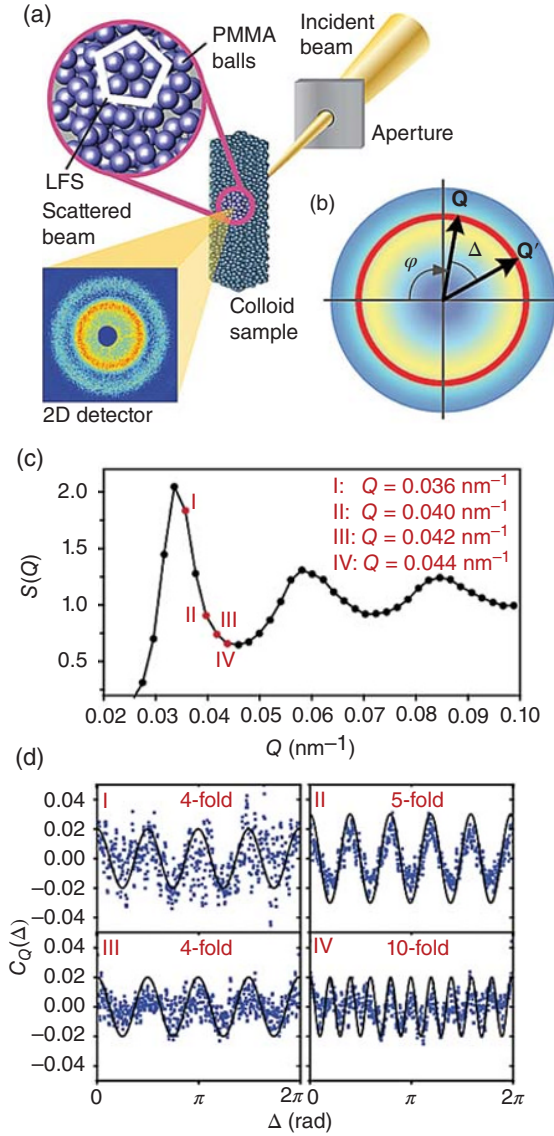
Figure 9. (a) A 10 μm partially coherent X-ray beam with a wavelength of 0.154 nm was defined by a collimating aperture. Speckle patterns are recorded by a charge-coupled device camera with 20 μm pixel size in 2265 mm distance. Series of 1000 CCD images were taken with exposure time of 0.15 s and for a diluted sample with 0.4 s. (b) Schematic intensity distribution with instructional guide for the construction of $C_Q(\Delta)$. (c) Angular averaged structure factor calculated from one of the measured diffraction patterns, which is the standard radial intensity distribution. (d) Experimental results after applying the cross-correlator $C_Q(\Delta)$ to the same diffraction pattern at different Q values. Solid lines are guide to the eyes. Wochner et al. [11]. Reproduced with permission of PNAS.

characterized by the BO-order parameters C_{6m} ($m = 1, 2, 3, \ldots$). They can be expressed using the coefficients of the Fourier cosine expansion of the scattered intensity [27, 30, 44, 45, 98],

$$I(q, \varphi) = I_0(q) + 2 \sum_{n=1}^{n=+\infty} |I_n(q)| \cos [n\varphi + \psi_n(q)], \qquad (33)$$

where only the Fourier components of the orders $n = 6m$ contribute to the Fourier decomposition. The hexatic BO-order parameters are defined at the momentum transfer value $q = q_0$ at which maxima of the sixfold scattering peaks are observed as follows:

$$C_n = |I_n(q_0)/I_0(q_0)|, \quad n = 6m \ (m = 1, 2, 3, \ldots). \qquad (34)$$

In the Fourier decomposition (33), $I_0(q)$ is the scattered intensity averaged over a scattering ring of a radius q, and $|I_n(q)|$ and $\psi_n(q)$ are the magnitude and phase of the n-th Fourier component.

Clearly, the two-point CCF $C(q, \Delta)$ is well suited for the BO-order studies, since its angular Fourier components $C_n(q)$ can be directly related to the BO-order parameters defined in Eqs. (33) and (34). From the Fourier decomposition given in Eq. (23a), one can extract the magnitudes of the sixfold Fourier components of intensity (see (23b)), and use them in Eq. (34) to determine the BO-order parameters. The advantage of this approach is that the Fourier components of CCFs can be directly averaged over a large number M of diffraction patterns measured from various regions of the sample, to determine the average properties of the BO order [27, 30].

The results of such analysis of X-ray data measured from a liquid crystal compound 3(10)OBC (n-propyl-4′-n-decyloxybiphenyl-4-carboxylate) (see for details Ref. [30]) are presented in Fig. 10. In this study, an exceptionally high number ($m = 25$) of the successive BO-order parameters has been determined in the hexatic phase by means of XCCA (Fig. 10a and b). Such strongly developed hexatic order allowed the authors to determine higher order correction terms in the scaling relation for the BO-order parameters predicted by the multicritical scaling theory (MCST) [45] over a full temperature range of the hexatic phase existence. The correlation between the number of nonzero BO-order parameters and the positional correlation length ξ (see Fig. 10c) directly indicates strong coupling between the BO order and positional order in the hexatic phase of 3(10)OBC film. Further X-ray cross-correlation studies of the hexatic phase are planned to get a deeper insight into the properties of this mysterious phase.

3.   *Structural Inhomogeneities in Semicrystalline Polymers*

In general, orientational order in the system may be defined in terms of the Fourier components $I_n(q)$ [or $C_n(q)$] of arbitrary orders, for example, $n = 2m$,
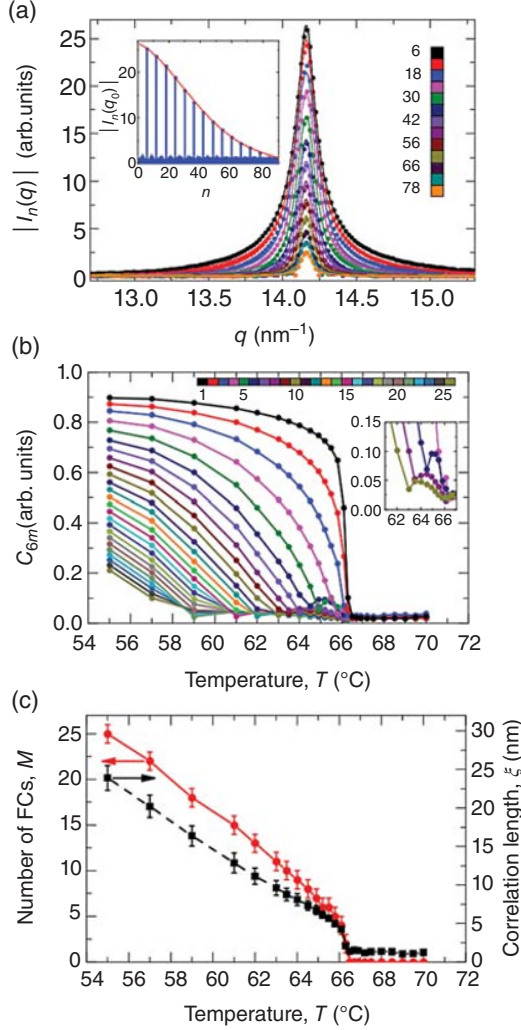
Figure 10. (a) Magnitudes of the FCs of intensity $|I_n(q)|$ with $n = 6, 12, \ldots, 78$ as a function of q at the temperature $T = 61.0°C$. Solid lines are square root Lorentzian and Lorentzian fits to the experimental data (points). (inset) Magnitudes of the FCs $|I_n(q)|$ at $q_0 = 14.16$ nm^{-1} as a function of the order n. Red line represents the fitting using the MCST. (b) Temperature dependence of the normalized BO-order parameters C_{6m}. In the inset, the nonmonotonic behavior of the BO-order parameters of the orders $m = 4, \ldots, 10$ is shown. (c) Temperature dependence of the total number of the nonzero measured FCs M and positional correlation length ξ. Zaluzhnyy et al. [30]. Reproduced with permission of American Physical Society. (*See insert for color representation of the figure.*)

$m = 1, 2, 3, \ldots$, depending on a particular structure of the material. Thus, the cross-correlation analysis of the X-ray nanodiffraction data from blends of poly(3-hexylthiophene) (P3HT) with gold NPs (AuNPs) revealed significant orientational order in the system (see Refs. [29, 93]), defined by pronounced contributions of the Fourier components of the orders $n = 2, 4, 6$ (see Fig. 11). In this study, to suppress the background scattering contribution, the two-point CCF of the form

$$C^{i,j}(q, \Delta) = \left\langle I^i(q, \varphi) I^j(q, \varphi + \Delta) \right\rangle_\varphi, \tag{35}$$

with the corresponding Fourier decomposition

$$C^{i,j}(q, \Delta) = \sum_{n=-\infty}^{\infty} C_n^{i,j}(q) \exp(in\Delta) \tag{36}$$

was applied, where $I^i(q, \varphi)$ and $I^j(q, \varphi)$ denote intensities measured on i-th and j-th diffraction patterns, respectively. The CCF $C^{i,j}(q, \Delta)$ and its Fourier components $C_n^{i,j}(q)$ in Eqs. (35) and (36) can be defined on two different diffraction patterns ($i \neq j$), or on the same diffraction pattern ($i = j$). The experimentally determined average spectrum $C_n^{i,i}(q)$ may contain both contributions, from the sample and from background scattering. To reduce the contribution of background in $C_n^{i,i}(q)$, the following ensemble-averaged difference spectrum has been used in the analysis [29, 93],

$$\langle \widetilde{C}_n(q) \rangle_M = \langle C_n^{i,i}(q) \rangle_M - \langle C_n^{i,j}(q) \rangle_M. \tag{37}$$

Such difference spectrum $\langle \widetilde{C}_n(q) \rangle_M$ was analyzed to quantify the degree of orientational order in semicrystalline P3HT blends [29, 93].

The difference spectrum shown in Fig. 11b indicates substantial orientational order of the crystalline domains (Fig. 11a) in the P3HT film [93]. Due to a smooth variation of the Fourier spectra of the CCFs over the scanned film area, it was possible to perform direct Fourier analysis of the diffraction patterns [29], and to determine the spatial distribution of the two predominant morphologies of P3HT domains (Fig. 11c), the face-on and edge-on (Fig. 11a). Detailed analysis of the spatial variation of the selected Fourier components of the CCFs also allowed to detect structural changes in the P3HT matrix induced by AuNPs (see Fig. 11d and e). This study demonstrates that X-ray beams focused to small sizes in combination with cross-correlation analysis can indeed provide valuable information about the structure of partially ordered materials, complementary to the results of conventional SAXS or grazing-incidence X-ray diffraction (GIXD) analysis.

4. *Short-Range and Medium-Range Order in Metallic Glasses*

The application of the X-ray cross-correlation techniques to study ordering phenomena in atomic systems, as it was envisioned by Clark et al., [2] is still
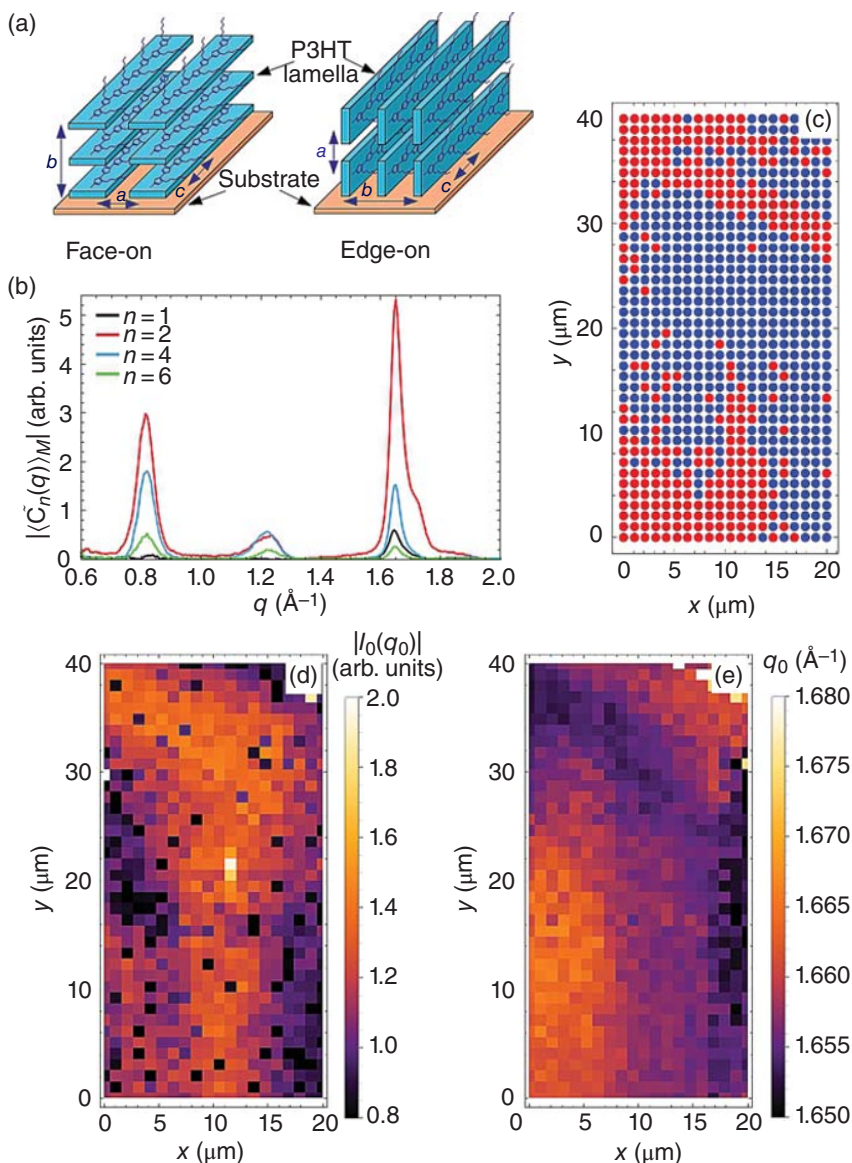
Figure 11.   (a) Two types of predominant orientation of semicrystalline P3HT domains with respect to a substrate: the face-on and edge-on orientations. (b) Magnitudes of the ensemble averaged Fourier components $|\langle \widetilde{C}_n(q)\rangle_M|$ of the difference spectrum (see text). (c) Two sample areas with predominant face-on (red points) and mixed (blue points) orientation of crystalline domains. (d and e) Spatially resolved 2D maps of the magnitude $|I_0(q_0)|$ of Au(111) peak (d), and position q_0 of the P3HT(002) peak (e), indicating significant correlation between these two values. Reproduced from Ref. [93]. Used under CC By 3.0, http://creativecommons.org/licenses/by/3.0/. Kurta et al. [29]. Reproduced with permission of Royal Society of Chemistry. (*See insert for color representation of the figure.*)

complicated. The lack of focusing optics, which produces a sufficiently small X-ray probe on the sample, and a weak cross-section of elastic X-ray scattering are two main reasons that make X-ray experiments from small scattering volumes of disordered systems extremely challenging. A typical lengthscale corresponding to MRO in metallic glasses is on the order of few nanometers [37, 101, 102], and is not accessible with the available focusing X-ray optics. At the same time, sufficient scattered signal can be measured from such small scattering volumes by means of electron diffraction. This particularly led to a development of fluctuation electron and X-ray microscopy techniques, which are based on the analysis of variance of the diffracted electron (X-ray) intensity, particularly of its dependence on the probe size [5, 101, 103–105].

Recently, a cross-correlation study of SRO and MRO in $Zr_{36}Cu_{64}$ glass has been done by means of scanning electron nanodiffraction (SEND) [33]. Through the statistical analysis of CCFs in experimental and simulated SEND patterns, it was demonstrated that the dominant SRO in a melt-spun $Zr_{36}Cu_{64}$ glass was consistent with icosahedral clusters. Analysis of the spatial extent of prominent angular symmetries in this work suggests a face-sharing or interpenetrating model of MRO in the glass.

5. Emergent Rotational Symmetries and Domain Memory in Magnetic Multilayers

CCFs appear to be a useful tool for studying magnetic structure of materials [22, 23, 106, 107]. A resonant soft X-ray scattering experiment on thin magnetic CoPd/IrMn heterostructures revealed a diverse array of hidden rotational symmetries about the magnetization axis (see Fig. 12) [23]. Performing systematic analysis of speckle diffraction patterns (Fig. 12a–f) by means of the normalized two-point CCF (see Eq. 2) for different values of applied magnetic field, the authors observed evolution of the dominant Fourier components of the CCF associated with different rotational symmetries in the system (Fig. 12g–j). These symmetries depend on the applied magnetic field, magnetization history, and the scattering vector. While various symmetries are observed in many individual diffraction images, they are broadly distributed and average out after accumulating CCFs over many magnetization cycles, which allows to assume that they do not arise from local structural order or microcrystallinity in the film [23]. These results suggest that it might be possible to change or control the symmetry of magnetic patterns by external field, and to understand the impact of the emergent mesoscale order on the functional properties of material.

The angular CCF in the form of Eq. (35) with ($i \neq j$) was also applied to study the q-dependent magnetic domain memory effects in Co/Pd multilayers [22]. Two sets of such functions were measured during many magnetization cycles. They are the "quasiautocorrelation function" (QACF), when i-th and j-th images are taken on the same field cycle, and the CCF, when i-th and j-th images were taken
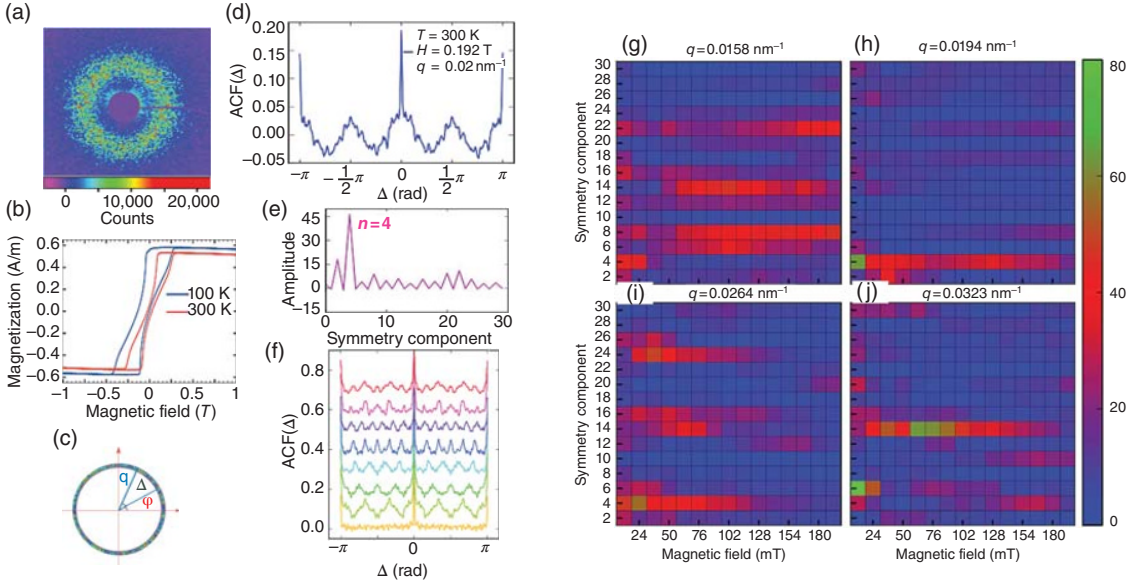
Figure 12. (a) Typical speckle diffraction pattern of the labyrinthine domain pattern of the CoPd/IrMn multilayer collected near the coercive field at $T = 300$ K. (b) Magnetization loops of the CoPd/IrMn multilayer collected at $T = 300$ K above the blocking temperature T_B (where the bias disappears) and at $T = 100$ K below T_B in a field cooled (FC) state. Note the leftward bias of the latter. (c) Annular region of the speckle pattern in (a) of nominal radius q in which a CCF is calculated. (d) CCF of the annular region in (c). (e) Cosine decomposition of the angular CCF in (d), showing a dominant component at $n = 4$. (f) Collection of several angular CCFs that exhibit the diverse hidden symmetries observed. (g–j) Maps of the spectrum of hidden symmetries observed (vertical) as a function of applied field (horizontal) along a single scan along the lower branch of the FC magnetization loop in (b) at values of q (g) below, (h) near, and (i and j) above $q = 0.02$ nm^{-1}. Su et al. [23]. Reprinted with permission from author Stephen D. Kevan, University of Oregon. (*See insert for color representation of the figure.*)

on different field cycles. The ratio of these two averaged functions was defined as a microscopic radial memory coefficient and used to quantify the magnetic memory [22],

$$\rho(q) = \frac{\sum_\Delta \text{QACF}(q, \Delta)}{\sum_\Delta \text{CCF}(q, \Delta)}, \tag{38}$$

where $\text{QACF}(q, \Delta)$ and $\text{CCF}(q, \Delta)$ are spline-normalized CCFs defined by Eq. (35). The observed peak in the systems memory $\rho(q)$ at $q = 0.0384$ nm^{-1} was attributed to bubble domains that nucleate reproducibly near initial field reversal and grow into a labyrinth domain structure that is not reproduced from one magnetization cycle to the next [22]. We would like to note that the different form of CCF (not angular CCFs as discussed before) was applied to study magnetic memory effects. It was defined as [106, 107]

$$I_1 \otimes I_2 = \sum_{q_x, q_y} I_1(q_x, q_y) I_2^*(-q_x + \delta q_x, -q_y + \delta q_y), \tag{39}$$

where I_1 and I_2 are the intensities of the respective images at pixel (q_x, q_y), and $(\delta q_x, \delta q_y)$ is the displacement of one image with respect to the other. Equation (39) can be used to correlate the entire diffraction patterns, or their portions in the form of a thin annulus to analyze the q-dependent memory effects [106, 107].

IV.   CONCLUSIONS AND OUTLOOK

In summary, it transpires that in the present state of the art, angular correlations provide a very effective tool for the investigation of systems in two dimensions, that is, in all cases in which the disorder is mainly related to a random orientation by rotation about a single axis, parallel to the direction of the incident X-rays (see Fig. 1). It implies on experimental side that development of reliable and widely applicable methods to align one axis of the molecule under investigation with reasonable accuracy could be an important step in application of XCCA methods to structural analysis on molecular level.

On the other hand, in cases when full 3D random rotations and orientations are present, the angular correlations seldom provide much new insight, unless some other previous knowledge of the system, such as information about its symmetry, is available *a priori*. This is the bottleneck on which future work should concentrate: from the theoretical point of view, the aim should be to improve our methods for disentangling 3D information; and on the experimental side, to devise reliable and widely applicable methods to align one axis of the molecule under investigation with reasonable accuracy. A recent publication [21] suggests that it can be possible to overcome these difficulties, and future progress in the theoretical analysis and experiment will demonstrate the capabilities of these new approaches.

At the same time from our review, it is also clear that XCCA can be used as a powerful tool for the analysis of condensed matter systems on different lengthscale and ordering. This is especially important with the developed nano-focused capabilities of high-brilliance synchrotron sources. As shown in this work XCCA can provide an important additional analysis tool to the portfolio of available techniques in order to get complementary information on the structure of the sample. At the same time, it is clear that it is still difficult to get information beyond the two-point pair correlation function by applying conventional angular intensity CCFs. In order to get access to higher order correlation functions, most probably different approaches would have to be applied.

With all this, we predict that in the coming years XCCA will develop to become an important analysis tool in scattering experiments applied to partially disordered systems with the use of high-brilliance synchrotron sources and X-ray free-electron lasers.

ACKNOWLEDGMENTS

REFERENCES

1. W. G. Griffin and P. N. Pusey, *Phys. Rev. Lett.* **43**, 1100 (1985).
2. N. A. Clark, B. J. Ackerson, and A. J. Hurd, *Phys. Rev. Lett.* **50**, 1459 (1983).
3. Z. Kam, *Macromolecules* **10**, 927 (1977).
4. A. Howie, C. A. McGill, and J. M. Rodenburg, *J. Phys.* **46**, 59 (1985).
5. J. M. Gibson, M. M. J. Treacy, T. Sun, and N. J. Zaluzec, *Phys. Rev. Lett.* **105**, 125504 (2010).
6. B. E. Warren, *X-Ray Diffraction* (Dover Publications, New York, 1990).
7. A. Guinier, *X-Ray Diffraction in Crystals, Imperfect Crystals, and Amorphous Bodies*, (Dover Publications, New York, 1994).
8. P. Emma *et al.*, *Nat. Photonics* **4**, 641 (2010).
9. T. Ishikawa *et al.*, *Nat. Photonics* **6**, 540 (2012).
10. M. Altarelli *et al.*, *The European X-Ray Free-Electron Laser - Technical Design Report* (DESY 2006-097, 2007).
11. P. Wochner, C. Gutt, T. Autenrieth, T. Demmer, V. Bugaev, A. Diaz-Ortiz, A. Duri, F. Zontone, G. Grübel, and H. Dosch, *Proc. Natl. Acad. Sci.* **106**, 11511 (2009).
12. M. Altarelli, R. P. Kurta, and I. A. Vartanyants, *Phys. Rev. B* **82**, 104207 (2010).
13. M. Altarelli, R. P. Kurta, and I. A. Vartanyants, *Phys. Rev.* B **86**, 179904 (2012).
14. V. Elser, *New J. Phys.* **13**, 123014 (2011).
15. D. K. Saldin, H. C. Poon, P. Schwander, M. Uddin, and M. Schmidt, *Opt. Express* **19**, 17318 (2011).

16. R. P. Kurta, M. Altarelli, E. Weckert, and I. A. Vartanyants, *Phys. Rev. B* **85**, 184204 (2012).
17. H. Liu, B. K. Poon, D. K. Saldin, J. C. H. Spence, and P. H. Zwart, *Acta Cryst. A* **69**, 365 (2013).
18. R. P. Kurta, R. Dronyak, M. Altarelli, E. Weckert, and I. A. Vartanyants, *New J. Phys.* **15**, 013059 (2013).
19. F. Lehmkühler, G. Grübel, and C. Gutt, *J. Appl. Cryst.* **47**, 1315 (2014).
20. T. Sun, M. M. J. Treacy, T. Li, N. J. Zaluzec, and J. M. Gibson, *Microsc. Microanal.* **20**, 627–634 (2014).
21. J. J. Donatelli, P. H. Zwart, and J. A. Sethian, *Proc. Natl. Acad. Sci.* **112**, 10286 (2015).
22. K. A. Seu, S. Roy, R. Su, D. H. Parks, E. Shipton, E. E. Fullerton, and S. D. Kevan, *Appl. Phys. Lett.* **98**, 122505 (2011).
23. R. Su, K. A. Seu, D. Parks, J. J. Kan, E. E. Fullerton, S. Roy, and S. D. Kevan, *Phys. Rev. Lett.* **107**, 257204 (2011).
24. D. K. Saldin, H. C. Poon, M. J. Bogan, S. Marchesini, D. A. Shapiro, R. A. Kirian, U. Weierstall, and J. C. H. Spence, *Phys. Rev. Lett.* **106**, 115501 (2011).
25. D. Starodub *et al.*, *Nat. Commun.* **3**, 1276 (2012).
26. B. Pedrini, A. Menzel, M. Guizar-Sicairos, V. A. Guzenko, S. Gorelick, C. David, B. D. Patterson, and R. Abela, *Nat. Commun.* **4**, 1647 (2013).
27. R. P. Kurta, B. I. Ostrovskii, A. Singer, O. Y. Gorobtsov, A. Shabalin, D. Dzhigaev, O. M. Yefanov, A. V. Zozulya, M. Sprung, and I. A. Vartanyants, *Phys. Rev. E* **88**, 044501 (2013).
28. D. Mendez, T. J. Lane, J. Sung, J. Sellberg, C. Levard, H. Watkins, A. E. Cohen, M. Soltis, S. Sutton, J. Spudich, V. Pande, D. Ratner, and S. Doniach, *Philos. Trans. R. Soc. B* **369**, 20130315 (2014).
29. R. P. Kurta, L. Grodd, E. Mikayelyan, O. Y. Gorobtsov, I. A. Zaluzhnyy, I. Fratoddi, I. Venditti, M. V. Russo, M. Sprung, I. A. Vartanyants, and S. Grigorian, *Phys. Chem. Chem. Phys.* **17**, 7404 (2015).
30. I. A. Zaluzhnyy, R. P. Kurta, E. A. Sulyanova, O. Y. Gorobtsov, A. G. Shabalin, A. V. Zozulya, A. P. Menushenkov, M. Sprung, B. I. Ostrovskii, and I. A. Vartanyants, *Phys. Rev. E* **88**, 044501 (2015).
31. M. A. Schroer, C. Gutt, F. Lehmkühler, B. Fischer, I. Steinke, F. Westermeier, M. Sprung, and G. Grübel, *Soft Matter* **11**, 5465 (2015).
32. M. A. Schroer, C. Gutt, and G. Grübel, *Phys. Rev. E* **90**, 012309 (2014).
33. A. C. Y. Liu, M. J. Neish, G. Stokol, G. A. Buckley, L. A. Smillie, M. D. de Jonge, R. T. Ott, M. J. Kramer, and L. Bourgeois, *Phys. Rev. Lett.* **110**, 205505 (2013).
34. D. K. Saldin, V. L. Shneerson, R. Fung, and A. Ourmazd, *J. Phys.: Condens. Matter* **21**, 134014 (2009).
35. P. J. Steinhardt, D. R. Nelson, and M. Ronchetti, *Phys. Rev. B* **28**, 784 (1983).
36. X. J. Liu, Y. Xu, X. Hui, Z. P. Lu, F. Li, G. L. Chen, J. Lu, and C. T. Liu, *Phys. Rev. Lett.* **105**, 155501 (2010).
37. H. W. Sheng, W. K. Luo, F. M. Alamgir, J. M. Bai, and E. Ma, *Nature* **439**, 419 (2006).
38. H. Shintani and H. Tanaka, *Nat. Phys.* **2**, 200 (2006).
39. T. Kawasaki, T. Araki, and H. Tanaka, *Phys. Rev. Lett.* **99**, 215701 (2007).
40. H. Tanaka, T. Kawasaki, H. Shintani, and K. Watanabe, *Nat. Mater.* **9**, 324 (2010).
41. Y. Q. Cheng and E. Ma, *Prog. Mater. Sci.* **56**, 379 (2011).
42. R. Pindak, D. E. Moncton, S. C. Davey, and J. W. Goodby, *Phys. Rev. Lett.* **46**, 1135 (1981).
43. R. Bruinsma and D. R. Nelson, *Phys. Rev. B* **23**, 402 (1981).
44. J. D. Brock, A. Aharony, R. J. Birgeneau, K. Evans-Lutterodt, J. D. Litster, P. M. Horn, G. B. Stephenson, and A. R. Tajbakhsh, *Phys. Rev. Lett.* **57**, 98 (1986).
45. A. Aharony, R. J. Birgeneau, J. D. Brock, and J. D. Litster, *Phys. Rev. Lett.* **57**, 1012 (1986).
46. R. P. Kurta, M. Altarelli, and I. A. Vartanyants, *Adv. Condens. Matt. Phys.* **2013**, 959835 (2013).
47. J. Als-Nielsen and D. McMorrow, *Elements of Modern X-ray Physics*, 2 nd edition (John Wiley & Sons, Ltd, Singapore, 2011).

48. Z. Kam, *J. Theor. Biol.* **82**, 15 (1980).
49. Z. Kam, I. Gafni, and M. Kessel, *Ultramicroscopy* **7**, 311 (1982).
50. Z. Kam and I. Gafni, *Ultramicroscopy* **17**, 251 (1985).
51. H. C. Poon, M. Schmidt, and D. K. Saldin, *Adv. Cond. Matt. Phys.* **2013**, 750371 (2013).
52. H. C. Poon, P. Schwander, M. Uddin, and D. K. Saldin, *Phys. Rev. Lett.* **110**, 265505 (2013).
53. H. Liu, B. K. Poon, A. J. E. M. Janssen, and P. H. Zwart, *Acta Cryst. A* **68**, 561–567 (2012).
54. Without loss of generality we fix the reference orientation to $\psi_0 = 0$.
55. A. V. Oppenheim, R. W. Sharfer, and J. R. Buck, *Discrete-Time Signal Processing* (Prentice Hall, *Upper Saddle River, NJ*, 1999).
56. J. Goodman, *Speckle Phenomena in Optics: Theory and Applications* (Roberts and Company Publishers, Englewood, CO, 2007).
57. D. K. Saldin, V. L. Shneerson, M. R. Howells, S. Marchesini, H. N. Chapman, M. Bogan, D. Shapiro, R. A. Kirian, U. Weierstall, K. E. Schmidt, and J. C. H. Spence, *New J. Phys.* **12**, 035014 (2010).
58. S. Ravy, *Acta Cryst. A* **69**, 543 (2013).
59. Z. Kam, M. H. J. Koch, and J. Bordas, *Proc. Nat. Acad. Sci.* **78**, 3559 (1981).
60. D. K. Saldin, H. C. Poon, V. L. Shneerson, M. Howells, H. N. Chapman, R. A. Kirian, K. E. Schmidt, and J. C. H. Spence, *Phys. Rev. B* **81**, 174105 (2010).
61. V. Elser, *Ultramicroscopy* **111**, 788 (2011).
62. G. Chen, M. A. Modestino, B. K. Poon, A. Schirotzek, S. Marchesini, R. A. Segalman, A. Hexemerc, and P. H. Zwart, *J. Synchrotron Radiat* **19**, 695–700 (2012).
63. E. Malmerberg, C. A. Kerfeld, and P. H. Zwart, *IUCrJ* **2**, 309 (2015).
64. S. A. Bobkov, A. B. Teslyuk, R. P. Kurta, O. Y. Gorobtsov, O. M. Yefanov, V. A. Ilyin, R. A. Senin, and I. A. Vartaniants, *J. Synchrotron Radiat* **22**, 1345 (2015).
65. S. Habermehl, P. Mörschel, P. Eisenbrandt, S. M. Hammer, and M. U. Schmidt, *Acta Cryst. B* **70**, 347 (2014).
66. K. J. Gaffney and H. N. Chapman, *Science* **316**, 1444 (2007).
67. A. P. Mancuso, O. M. Yefanov, and I. A. Vartanyants, *J. Biotechnol.* **149**, 229 (2010).
68. M. M. Seibert *et al.*, *Nature* **470**, 78 (2011).
69. R. Neutze, R. Wouts, D. van der Spoel, E. Weckert, and J. Hajdu, *Nature* **406**, 752 (2000).
70. U. Lorentz, N. M. Kabachnik, E. Weckert, and I. A. Vartanyants, *Phys. Rev. E* **86**, 051911 (2012).
71. B. Ziaja, H. N. Chapman, R. Fäustlin, S. Hau-Riege, Z. Jurek, A. V. Martin, S. Toleikis, F. Wang, and E. Weckert, *New J. Phys.* **14**, 115015 (2012).
72. J. M. Slowik, S.-K. Son, G. Dixit, Z. Jurek, and R. Santra, *New J. Phys.* **16**, 073042 (2014).
73. O. Y. Gorobtsov, U. Lorentz, N. M. Kabachnik, and I. A. Vartanyants, *Phys. Rev. E* **91**, 062712 (2015), accepted.
74. H. N. Chapman *et al.*, *Nature* **470**, 73 (2011).
75. S. Boutet *et al.*, *Science* **337**, 362 (2012).
76. H. C. Poon and D. K. Saldin, *Ultramicroscopy* **111**, 798 (2011).
77. J. R. Fienup, *Appl. Opt.* **21**, 2758 (1982).
78. V. Elser, *J. Opt. Soc. Am.* **20**, 40 (2003).
79. S. Marchesini, *Rev. Sci. Instrum.* **78**, 011301 (2007).
80. J. R. Fienup, *Appl. Opt.* **52**, 45 (2013).
81. R. A. Kirian, K. E. Schmidt, X. Wang, R. B. Doak, and J. C. H. Spence, *Phys. Rev. E* **84**, 011921 (2011).
82. R. A. Kirian, *J. Phys. B: At., Mol. Opt. Phys.* **45**, 223001 (2012).
83. R. P. Kurta, Y. Chesnokov, E. Weckert, and I. A. Vartanyants, *J. Phys: Conf. Ser.* **463**, 012046 (2013).
84. G. Oszlányi and A. Sütő, *Acta Cryst. A* **64**, 123 (2007).
85. O. M. Yefanov and I. A. Vartanyants, *J. Phys. B: At., Mol. Opt. Phys.* **46**, 164013 (2013).
86. D. I. Svergun and H. B. Stuhrmann, *Acta Cryst.* **47**, 736 (1991).

87. V. L. Shneerson and D. K. Saldin, *Acta Cryst.* **65**, 128–134 (2009).

88. D. R. Luke, *Inverse Probl.* **21**, 37–50 (2005).

89. R. L. McGreevy and L. Pusztai, *Mol. Simul.* **1**, 359 (1988).

90. G. Chen, P. H. Zwart, and D. Li, *Phys. Rev. Lett.* **110**, 195501 (2013).

91. B. J. Ackerson and N. A. Clark, *Faraday Discuss. Chem. Soc.* **76**, 219 (1983).

92. P. N. Pusey and J. G. Rarity, *J. Phys.* **46**, 43 (1985).

93. R. P. Kurta, L. Grodd, E. Mikayelyan, O. Y. Gorobtsov, I. Fratoddi, I. Venditti, M. Sprung, S. Grigorian, and I. A. Vartanyants, *J. Phys.: Conf. Ser.* **499**, 012021 (2014).

94. B. J. Ackerson, T. W. Taylor, and N. A. Clark, *Phys. Rev. A* **31**, 3183 (1985).

95. A. S.-Y. Sheu and S. Rice, *J. Chem. Phys.* **128**, 244517 (2008).

96. A. S.-Y. Sheu and S. Rice, *J. Chem. Phys.* **129**, 124511 (2008).

97. B. I. Halperin and D. R. Nelson, *Phys. Rev. Lett.* **41**, 121 (1978).

98. J. D. Brock, R. J. Birgeneau, D. Litster, and A. Aharony, *Contemp. Phys.* **30**, 321 (1989).

99. W. H. de Jeu, B. I. Ostrovskii, and A. N. Shalaginov, *Rev. Mod. Phys.* **75**, 181 (2003).

100. K. J. Strandburg, ed., *Bond-Orientational Order in Condensed Matter Systems*, Partially Ordered Systems (Springer-Verlag, New York, 1992).

101. M. M. J. Treacy, D. Kumar, A. Rougee, G. Zhao, P. Buseck, I. McNulty, L. Fan, C. Rau, and J. M. Gibson, *J. Phys.: Condens. Matter* **19**, 455201 (2007).

102. G. Baldi, M. Zanatta, E. Gilioli, V. Milman, K. Refson, B. Wehinger, B. Winkler, A. Fontana, and G. Monaco, *Phys. Rev. Lett.* **110**, 185503 (2013).

103. M. M. J. Treacy, J. M. Gibson, L. Fan, D. J. Paterson, and I. McNulty, *Rep. Prog. Phys.* **68**, 2899–2944 (2005).

104. L. Fan, D. Paterson, I. McNulty, M. M. J. Treacy, and J. M. Gibson, *J. Microsc.* **225**, 41 (2007).

105. M. M. J. Treacy and K. B. Borisenko, *Science* **335**, 950 (2012).

106. K. Chesnel, J. A. Nelson, M. J. Carey, and E. E. Fullerton, *Phys. Rev. B* **83**, 054436 (2011).

107. K. Chesnel, J. Nelson, B. Wilcken, and S. D. Kevan, *J. Synchrotron Radiat.* **19**, 293–306 (2012).

SPIN RELAXATION IN PHASE SPACE

YURI P. KALMYKOV[1], WILLIAM T. COFFEY[2], and SERGUEY V. TITOV[3]

[1]*Laboratoire de Mathématiques et Physique (LAMPS, EA 4217), Université de Perpignan Via Domitia, Perpignan, France*
[2]*Department of Electronic and Electrical Engineering, Trinity College, Dublin, Ireland*
[3]*Kotel'nikov Institute of Radio Engineering and Electronics of the Russian Academy of Sciences, Moscow, Russian Federation*

CONTENTS

I. INTRODUCTION

The interpretation of spin relaxation experiments comprises a fundamental problem of condensed phase physics and chemistry, yielding a well-defined means of extracting information concerning the spin dynamics in gases, liquids, and solids, so providing a bridge between microscopic and macroscopic physics. For example, since the number of spins in a sample roughly corresponds to the number of atoms, on an *atomic* level, nuclear magnetic and related spin resonance experiments, and so on, examine the time evolution of the individual *elementary* spins [1, 2] of nuclei, electrons, muons, and so on, while on *mesoscales* the time evolution of magnetic *molecular clusters* (i.e., spins 15–25 μ_B) exhibiting relatively large quantum effects is relevant to the fabrication of molecular magnets [3]. On *nanoscales* single domain ferromagnetic particles (giant spins 10^4–10^5 μ_B) with a given orientation of the particle moment and permanent magnetization exist. These have spawned very extensive magnetic recording industries, the particles commonly used being on or near the microsize scale. Also on a *nanoscale* level, we have magnetic fluids composed of single domain ferromagnetic particles in a

colloidal suspension. Here, relaxation experiments detect [4, 5] both the Arrhenius or solid-state-like (Néel) mechanism [6] of relaxation of the magnetization, which may be overcome via thermal agitation anisotropy potential barriers inside the particle and the Debye orientational relaxation [7, 8] due to physical Brownian rotation of the suspended particles in the presence of thermal agitation. Here, quantum effects are expected to be much smaller. Finally, on the *bulk macroscopic scale*, permanent magnets (10^{20} μ_B) exist, that is, *multi-domain* systems, where magnetization reversal occurs via the *macroscopic* processes of nucleation, propagation, and annihilation of domain walls. Thus, a *well-defined spin number scale* ranging from the bulk macroscopic down to individual atom and spins naturally occurs [9] (see Fig. 1).

On an atomic-level, spin relaxation experiments in nuclear magnetic or electron spin resonance are usually interpreted via the phenomenological Bloch [10] equations and their later modifications [1, 2] pertaining to the relaxation of elementary spins subjected to an external magnetic field and interacting with an environment constituting a heat reservoir at constant temperature T. These simple linear equations of motion for the nuclear magnetization were originally proposed on phenomenological grounds. The main assumption is that the effects of the heat bath can be described two different time constants: the so-called T1 and T2 relaxation times. They provide a substantially correct quantitative description
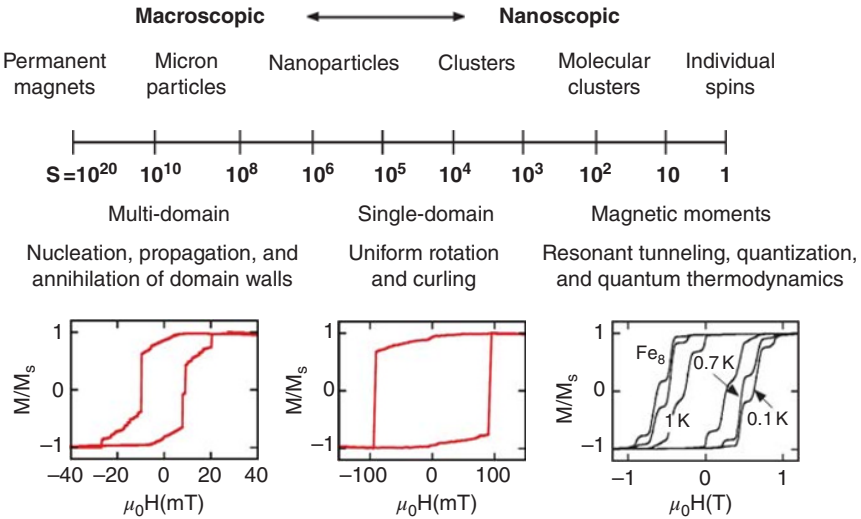

Figure 1. The transition from macroscopic to nanoscopic magnets. The hysteresis loops are typical examples of magnetization reversal via nucleation, propagation, and annihilation of domain walls (left), via uniform rotation (middle), and via quantum tunneling (right). Wernsdorfer [9], Reproduced with permission of John Wiley & Sons, Inc. (Color on line).

for liquid samples [1]. Microscopic theories of the relaxation in quantum spin systems have been developed by Bloch [11], Bloembergen, et al. [12], and other authors (see, e.g., Refs. 13–15). These microscopic theories have provided general evolution equations for the density matrix operator of the spin system allowing one, in principle, to evaluate all desired observables such as relaxation times, and so on.

On meso- and nanoscales, both the behavior of the hysteresis loop and the reversal time of the magnetization of molecular clusters and nanomagnets are essential for observation of the transition from the macroscopic to the nanoscale level as quantum effects are likely to occur as the spin number decreases (see Fig. 1). In this region, the magnetization in molecular nanomagnets may reverse both due to thermal agitation and quantum tunneling as may be observed in the corresponding hysteresis loop [9]. In contrast, in single, domain ferromagnetic nanoparticles (originally encountered in paleomagnetism in the context of past reversals of the Earth's magnetic field, where depending on the volume of the particle, the relaxation time may vary from nanoseconds to millions of years), the magnetization reversal is treated classically by assuming *uniform* rotation of the magnetization vector as conjectured by Néel [16] and Stoner and Wohlfarth [17]. The relaxation time epochs represent the transition from Langevin paramagnetic behavior of nanoparticles (superparamagnetism) with no hysteresis involved via the magnetic after-effect stage, where the magnetization reversal time is of the order of the time of a measurement, to stable ferromagnetism. There a given ferromagnetic state that corresponds to one of many possible such metastable states in which the magnetization vector is held in a preferred orientation. In the hypothesis of uniform or coherent rotation, the exchange interactions render all atomic spins collinear and the magnitude of the magnetization vector is constant in space. This hypothesis should hold for fine (nanometric) magnetic particles, where domain walls cannot form in the sample because it is energetically unfavorable.

The *static* magnetization properties of single, domain particles are usually treated via the method given by Stoner and Wohlfarth [17]. Their procedure simply consists in *minimizing the free energy of the particle*, that is, the sum of the Zeeman and anisotropy energies with respect to the polar and azimuthal angles specifying the orientation of the magnetization for each value of the applied field. The calculation always leads to hysteresis because in certain field ranges, two or more minima exist and thermally agitated transitions between them are neglected. The value of the applied field, at which the magnetization reverses, is called the *switching field* and the *angular dependence of that field with respect to the easy axis of the magnetization* yields the well-known Stoner–Wohlfarth astroids [17, 18]. These were originally given for uniaxial shape anisotropy only, which is the anisotropy of the magnetostatic energy of the sample induced by its nonspherical shape. The astroids represent a parametric plot of the parallel versus the perpendicular component of the switching field, which in the uniaxial case is